

The onset of instability in unsteady boundary-layer separation

By K. W. CASSEL¹, F. T. SMITH² AND J. D. A. WALKER¹

¹Department of Mechanical Engineering and Mechanics, Lehigh University,
19 Memorial Drive West, Bethlehem, PA 18015, USA

²Department of Mathematics, University College London, Gower Street, London WC1E 6BT, UK

(Received 1 March 1994 and in revised form 18 September 1995)

The process of unsteady two-dimensional boundary-layer separation at high Reynolds number is considered. Solutions of the unsteady non-interactive boundary-layer equations are known to develop a generic separation singularity in regions where the pressure gradient is prescribed and adverse. As the boundary layer starts to separate from the surface, however, the external pressure distribution is altered through viscous–inviscid interaction just prior to the formation of the separation singularity; hitherto this has been referred to as the first interactive stage. A numerical solution of this stage is obtained here in Lagrangian coordinates. The solution is shown to exhibit a high-frequency inviscid instability resulting in an immediate finite-time breakdown of this stage. The presence of the instability is confirmed through a linear stability analysis. The implications for the theoretical description of unsteady boundary-layer separation are discussed, and it is suggested that the onset of interaction may occur much sooner than previously thought.

1. Introduction

At high Reynolds numbers, fluid particles within a boundary layer experience a momentum deficit relative to the external mainstream flow and are very susceptible to separation in regions of adverse external pressure gradient. In such circumstances a local and abrupt eruption of boundary-layer fluid is often observed in which vorticity is first concentrated within the boundary layer into a band which is very narrow in the streamwise direction, and then ejected into the mainstream in a strong viscous–inviscid interaction (Doligalski, Smith & Walker 1994). The adverse pressure gradient which initiates this process may be due to the surface geometry or a vortex convecting above the surface, but the end result is a localized breakdown and boundary-layer eruption. Such events are common in a variety of large-scale applications such as turbomachinery and various airfoil flows (McCroskey 1982; Smith 1982). At small scales, transition and turbulence are known to be provoked by the effects of vortex motion, wherein new turbulence is generated and sustained by local eruptions of wall-layer vorticity caused by the convection of hairpin vortices near the surface (Head & Bandyopadhyay 1981; Acarlar & Smith 1987*a,b*; Smith *et al.* 1991; Walker 1990).

Because unsteady separation is prevalent in most flows near solid walls at high Reynolds numbers, there has been intense interest for many years in understanding the physical processes and in developing a theoretical explanation of the phenomena involved. In order to facilitate such an investigation, two model problems have been

studied extensively: the impulsively started circular cylinder and the rectilinear vortex above a plane wall. Many numerical studies of the impulsively started circular cylinder (see, for example, Collins & Dennis 1973; Cebeci 1982) accurately predict the flow development for early times and compare well with experimental investigations (Bouard & Coutanceau 1980). However, severe numerical difficulties were invariably experienced in all cases when an extension of the solution for larger times was sought. Similar difficulties were encountered at larger times by Walker (1978) (see also Doligalski & Walker 1984) in the computation of the boundary-layer evolution induced by a two-dimensional vortex. Common in these and other studies is the formation of a growing reversed flow region in the boundary layer; eventually, a narrow region forms just upstream of the recirculation zone where dramatic increases in boundary-layer thickness and displacement velocity are observed just prior to failure of the numerical algorithm.

Sears & Telionis (1975) argued that the source of these numerical difficulties is that a singularity is forming in the solution of the non-interactive boundary-layer equations, and this event signals an eventual breakdown of the concept of a thin boundary layer attached to the surface. They suggested that 'separation' should be defined as corresponding to the evolution of this singularity and postulated the MRS model of unsteady separation. This model specifies two necessary conditions that must apply at separation: (i) the separation point must move with the local flow speed (MRS I) and (ii) the separation point must be located somewhere along a line of zero vorticity (MRS II). Boundary-layer flows that develop recirculation zones will contain a zero-vorticity line and consequently are highly susceptible to separation at subsequent times. Early attempts to verify the MRS model were hampered by the substantial problems associated with calculating accurate numerical solutions in a conventional Eulerian formulation as a boundary layer starts to develop strong outflows.

The numerical problem was resolved by Van Dommelen & Shen (1980, 1982) who obtained solutions of the boundary-layer equations in Lagrangian coordinates for the impulsively started cylinder problem. In this approach the trajectories of individual fluid particles are evaluated, and the formulation decouples the solution of the streamwise momentum equation from that of the continuity equation. The streamwise momentum equation involves only the streamwise particle positions x and their velocities u , both of which remain regular even as a boundary layer starts to erupt. An additional advantage of Lagrangian coordinates is that there is an unambiguous criterion for the formation of a singularity, which occurs in the solution of the continuity equation. Van Dommelen & Shen (1980, 1982) definitively showed that a singularity forms at finite time for the cylinder problem in the form of a sharply focused eruption. Subsequently, similar behaviour was found by Peridier, Smith & Walker (1991*a*) for vortex-induced separation.

The analytical form of the terminal boundary-layer structure for two-dimensional flows was determined by Van Dommelen & Shen (1982) and Elliott, Cowley & Smith (1983), and this will be described briefly in §2. It was shown that as the singularity evolves, the boundary layer bifurcates into two passive shear layers above and below an intermediate vorticity-depleted region, which grows explosively in a direction normal to the surface but thins in the streamwise direction. This process results in a pronounced streamwise compression of fluid particles near separation and the consequent development of a spike in the displacement thickness. An important characteristic of the terminal state is that it is independent of the specific form of the external adverse pressure gradient that initiated the eruptive process at some earlier time. Therefore, this terminal structure is believed to be generic and to apply to most cases of unsteady boundary-layer eruptions in two-dimensional incompressible flow.

The singularity in the terminal solution arises as a consequence of attempting to impose the mainstream pressure gradient on the boundary layer for an indefinite period of time within the context of a non-interactive formulation. However, the terminal solution describes locally a rapidly thickening boundary layer which must at some point begin to alter the outer flow. The resulting viscous-inviscid interaction may be dealt with in two ways. In a limit analysis for large Reynolds numbers, the new scalings and regions that occur with the advent of interaction just prior to the non-interactive singularity time are determined. This has been carried out by Elliott *et al.* (1983) and yields a problem which to date was believed to be the *first* interactive stage; a description of this stage will be given in §3, and numerical solutions of the problem will be described in §4 and §5. In this stage the intermediate vorticity-depleted region develops under the influence of a pressure gradient induced by the thickening boundary layer, and the governing equations are nonlinear and inviscid.

An alternative approach is interacting boundary-layer theory wherein a large, but finite, value of the Reynolds number is assumed, and the boundary-layer solutions are obtained with a pressure distribution evaluated through an interaction condition relating pressure to the displacement thickness. This approach has been used by Henkes & Veldman (1987), Chuang & Conlisk (1989), Riley & Vasantha (1989) and Peridier, Smith & Walker (1991*b*) to compute the impulsively started circular cylinder problem and vortex-induced boundary-layer separation, but with contradictory results. Henkes & Veldman (1987) indicate a delay in the onset of breakdown when interaction is taken into account, while Riley & Vasantha's (1989) calculations did not seem to become singular at all. On the other hand, Peridier *et al.* (1991*b*), using Lagrangian coordinates for vortex-induced separation, found that interacting boundary-layer theory actually produced a singularity at a time earlier than that computed without interaction. The calculations of Peridier *et al.* (1991*b*) also appeared to corroborate the scalings found by Elliott *et al.* (1983) for the first interactive stage, as well as the theory of Smith (1988) who discovered a possible breakdown and singularity in the interacting boundary-layer formulation.

In the present study a numerical solution of the so-called first interactive stage is described. The problem as formulated by Elliott *et al.* (1983) in Eulerian coordinates is virtually intractable for numerical solution and was reformulated here in Lagrangian coordinates in §3. Numerical methods and calculated results are given in §4 and §5, respectively. The results reveal the presence of a high-frequency instability in the first interactive stage. The instability is of an inviscid type with very high growth rates and is closely related to that described by Brown, Cheng & Smith (1988); its presence in the first interactive stage is confirmed through a linear stability analysis described in §6. The implications of these results for unsteady separation theory are discussed in §7. In particular it is tentatively suggested that interactive breakdown and the development of a singularity generally may occur at a time well ahead of the non-interactive singularity time, or in other words, well before the so-called 'first' interactive stage is entered.

2. Terminal boundary-layer structure

2.1. Form of the terminal singularity

The numerical results of Van Dommelen & Shen (1980) showed that a singularity can occur in the boundary-layer equations within a finite time, and this prompted Van Dommelen & Shen (1982) and Elliott *et al.* (1983) to seek a local analytical description which is referred to here as the terminal boundary-layer structure. Van Dommelen

& Shen (1982) hypothesized that the solution for the streamwise particle positions in Lagrangian coordinates should remain regular up to the time of separation; therefore, a local Taylor series expansion for the solution of the momentum equation near the point of separation was constructed, and the solution of the continuity equation (which becomes singular) was represented as an asymptotic series (see also Cowley, Van Dommelen & Lam 1990). An alternative derivation due to Elliott *et al.* (1983) reproduced the same structure in Eulerian coordinates; a brief summary of this approach follows.

Let (x, y) be streamwise and normal coordinates with corresponding velocities (u, v) , and define scaled boundary-layer variables by $Y = Re^{1/2}y$ and $V = Re^{1/2}v$. The unsteady incompressible boundary-layer equations are

$$\frac{\partial u}{\partial t} + u \frac{\partial u}{\partial x} - \frac{\partial \psi}{\partial x} \frac{\partial u}{\partial Y} = -\frac{dp_e}{dx} + \frac{\partial^2 u}{\partial Y^2}, \quad (2.1)$$

where ψ is a streamfunction defined by $u = \partial\psi/\partial Y$, $V = -\partial\psi/\partial x$, and $p_e(x)$ is the mainstream pressure distribution. Assuming that a singularity develops at $x = x_s$ and for time $t = t_s$, a temporal similarity solution is sought as $t \rightarrow t_s$ in the immediate vicinity of the separation point. Consider the following scaled variables:

$$x = x_s + K(t_s - t) + (t_s - t)^M \tilde{X}, \quad Y = (t_s - t)^{-N} \tilde{Y}, \quad (2.2a, b)$$

where K , M and N are positive constants, and \tilde{X} and \tilde{Y} are $O(1)$. These variables describe a moving coordinate system which drifts upstream with constant velocity $-K$ with the origin arriving at the separation point x_s at time t_s . In accordance with the numerical solutions of Van Dommelen & Shen (1980, 1982) (see also Peridier *et al.* 1991a), this region thins in the streamwise direction and grows explosively in the normal direction as $t \rightarrow t_s$. Since the Lagrangian streamwise velocity has $\partial x/\partial t = u$, it follows that u and ψ are of the form

$$u = -K + (t_s - t)^{M-1} \tilde{U}(\tilde{X}, \tilde{Y}) + \dots, \quad (2.3a)$$

$$\psi = -K(t_s - t)^{-N} \tilde{Y} + (t_s - t)^{M-N-1} \tilde{\Psi}(\tilde{X}, \tilde{Y}) + \dots, \quad (2.3b)$$

where $\tilde{U}(\tilde{X}, \tilde{Y}) = \partial\tilde{\Psi}/\partial\tilde{Y}$ is $O(1)$. Equation (2.3a) is a statement of the MRS conditions for upstream-slipping separation, viz. $u = -K$ and $\partial u/\partial Y \rightarrow 0$ as $t \rightarrow t_s$; it is evident from equation (2.3a) that $M > 1$.

Substitution of the transformations (2.2) and (2.3) into equation (2.1) shows that the viscous term is negligible with respect to the pressure gradient term, and the balance is inviscid to leading order. A balance between the unsteady convection terms and the pressure gradient is possible if $M = 2$, but solutions where $1 < M < 2$ represent a larger longitudinal streamwise scale and will dominate if they exist; in the latter case the inertial terms dominate the pressure gradient, and the boundary-layer equations become

$$-(M-1)\tilde{U} + M\tilde{X} \frac{\partial \tilde{U}}{\partial \tilde{X}} - N\tilde{Y} \frac{\partial \tilde{U}}{\partial \tilde{Y}} + \tilde{U} \frac{\partial \tilde{U}}{\partial \tilde{X}} - \frac{\partial \tilde{\Psi}}{\partial \tilde{X}} \frac{\partial \tilde{U}}{\partial \tilde{Y}} = 0, \quad \tilde{U} = \frac{\partial \tilde{\Psi}}{\partial \tilde{Y}}, \quad (2.4a, b)$$

constituting a first-order nonlinear equation for $\tilde{U}(\tilde{X}, \tilde{Y})$, which is independent of the mainstream pressure gradient. Generally, the presence of an adverse pressure gradient initiates an eruptive process locally near x_s ; however, the singular flow structure which eventually forms in the solution of the boundary-layer equations is apparently generic with the leading-order terminal solution 'forgetting' the initiating pressure gradient. Solutions to equations (2.4) were originally obtained by Elliott *et*

al. (1983); an alternative approach is described in Appendix A where it is shown that

$$\tau = \frac{\partial \tilde{U}}{\partial \tilde{Y}} = \pm \frac{|\tilde{U}|^{1+N/(M-1)}}{G(\phi)}, \quad \phi = \frac{|\tilde{U}|^{M/(M-1)}}{|\tilde{U} + \tilde{X}|}, \quad (2.5a, b)$$

where G is a strictly positive function, but is otherwise arbitrary. Integration for fixed \tilde{X} yields

$$\tilde{Y} - \tilde{Y}_0(\tilde{X}) = \text{sgn}(\tau) \int_{\tilde{U}_0(\tilde{X})}^{\tilde{U}} G(\phi) |\tilde{U}|^{-[1+N/(M-1)]} d\tilde{U}, \quad (2.6)$$

where $\tilde{Y} = \tilde{Y}_0(\tilde{X})$ is the normal location where $\tau = 0$ and the velocity \tilde{U} is a minimum denoted by $\tilde{U}_0(\tilde{X})$. It follows from equations (2.5) that $\tau = 0$ at some positive value of $\phi = \phi_0$ where $G(\phi) \rightarrow \infty$, and the characteristic curve of equation (2.4) defining the line where $\tau = 0$ is given by $\phi_0 = |\tilde{U}_0|^{M/(M-1)} / |\tilde{U}_0 + \tilde{X}|$; this defines \tilde{U}_0 in terms of \tilde{X} , but different branches are possible depending on the sign of \tilde{U}_0 and $\tilde{U}_0 + \tilde{X}$. In order for $\tilde{U}_0(\tilde{X})$ to be a single-valued function of \tilde{X} , only the following branches are possible:

$$\tilde{U}_0^{M/(M-1)} + \phi_0(\tilde{U}_0 + \tilde{X}) = 0 \quad \text{for} \quad \tilde{U}_0 > 0, \tilde{U}_0 + \tilde{X} < 0, \quad (2.7a)$$

$$(-\tilde{U}_0)^{M/(M-1)} - \phi_0(\tilde{U}_0 + \tilde{X}) = 0 \quad \text{for} \quad \tilde{U}_0 < 0, \tilde{U}_0 + \tilde{X} > 0. \quad (2.7b)$$

Since $M > 1$, it follows from equations (2.7) that $\tilde{U}_0 \sim -\tilde{X}$ as $\tilde{X} \rightarrow 0$. Consequently, the exponent $M/(M-1)$ must be an integer greater than one since otherwise an expansion of \tilde{U}_0 about $\tilde{X} = 0$ would not be regular. Furthermore, $M/(M-1)$ must be odd in order to have a unique $\tilde{U}_0(\tilde{X})$ for each \tilde{X} , and it follows that equations (2.7) may be rewritten

$$\tilde{U}_0^{M/(M-1)} + \phi_0(\tilde{U}_0 + \tilde{X}) = 0, \quad \phi_0 > 0. \quad (2.8)$$

The choices of M for the streamwise scale on x are thus narrowed to $M = 3/2, 5/4, 7/6, \dots$, which all lie in the range $1 < M < 2$ as anticipated.

Near the centreline ϕ may be expanded in a Taylor series, and from equation (2.5b)

$$\phi - \phi_0 = -(\tilde{U} - \tilde{U}_0)\phi_0^2 \tilde{U}_0^{(1-2M)/(M-1)} \frac{M\tilde{X} + \tilde{U}_0}{M-1} + \dots \quad (2.9)$$

Since $G \rightarrow \infty$ as $\phi \rightarrow \phi_0$, assume that $G \sim G_1(\phi - \phi_0)^{-q_1}$, where q_1 is to be determined. An expansion of the integral in equation (2.6) about $\tilde{Y} = \tilde{Y}_0$ (where $\tilde{U} = \tilde{U}_0$) yields

$$\tilde{Y} - \tilde{Y}_0 = \pm(\tilde{U} - \tilde{U}_0) |\tilde{U}_0|^{-[1+N/(M-1)]} \frac{G_1}{(\phi - \phi_0)^{q_1}} + \dots \quad (2.10)$$

Using equation (2.9) in (2.10), it follows that $\tilde{U} - \tilde{U}_0 = O[(\tilde{Y} - \tilde{Y}_0)^{1/(1-q_1)}]$. However, since a minimum is assumed at $\tilde{Y} = \tilde{Y}_0$, it follows that $\tilde{U} - \tilde{U}_0 = O[(\tilde{Y} - \tilde{Y}_0)^2]$ near \tilde{Y}_0 ; consequently, $q_1 = 1/2$ and equation (2.10) becomes

$$\tilde{Y} - \tilde{Y}_0 = \pm \frac{G_1}{\phi_0} (M-1)^{1/2} \left(\frac{\tilde{U} - \tilde{U}_0}{M\tilde{X} + \tilde{U}_0} \right)^{1/2} |\tilde{U}_0|^{-[1+N/(M-1)]} \tilde{U}_0^{(2M-1)/[2(M-1)]} + \dots \quad (2.11)$$

Rewriting this expression in terms of $\tilde{U} - \tilde{U}_0$ and using $\tilde{U}_0 \sim -\tilde{X}$ as $\tilde{X} \rightarrow 0$, it is easily shown that

$$\tilde{U} - \tilde{U}_0 = \frac{\phi_0^2}{G_1^2} \tilde{X} |\tilde{X}|^{(2N-1)/(M-1)} (\tilde{Y} - \tilde{Y}_0)^2 + \dots, \quad \tilde{X} \rightarrow 0. \quad (2.12)$$

Thus, to avoid an irregularity at $\tilde{X} = 0$, $(2N - 1)/(M - 1) = -1, 0, 1, 2, \dots$, giving an infinite number of possibilities for the scales M and N in equations (2.2). The lowest-order singularity, having the slowest boundary-layer growth rate and hence the smallest value of N , has $M = 3/2$ and therefore $N = 1/4$.

The simplest function G satisfying the necessary requirements at ϕ_0 and which is bounded and non-zero as $\phi \rightarrow 0$ or $\phi \rightarrow \infty$ is given by $G(\phi) = A\phi^{1/2}(\phi - \phi_0)^{-1/2}$, where A is a constant; the latter conditions on G are required through considerations of the nature of the solution at the top and bottom of the domain. It may be noted that this form of G can also be obtained from an argument discussed by Van Dommelen (1981) which requires regularity in the Lagrangian solution for the streamwise particle positions x and velocities u (see also Cowley *et al.* 1990).

The constants ϕ_0 and A may be scaled out of the equations by redefining the transformation in equations (2.2) and (2.3) according to

$$x = x_s + K(t_s - t) + (t_s - t)^{3/2}\phi_0^{1/2}\tilde{X}, \quad Y = (t_s - t)^{-1/4}A\phi_0^{-1/4}\tilde{Y}, \quad (2.13a, b)$$

$$u = -K + (t_s - t)^{1/2}\phi_0^{1/2}\tilde{U}(\tilde{X}, \tilde{Y}) + \dots, \quad (2.13c)$$

and equations (2.5) and (2.6) become

$$\tau = \frac{\partial \tilde{U}}{\partial \tilde{Y}} = \pm(\tilde{U}^3 + \tilde{U} + \tilde{X})^{1/2}, \quad \tilde{Y} - \tilde{Y}_0 = \text{sgn}(\tau) \int_{\tilde{U}_0}^{\tilde{U}} \frac{d\tilde{U}}{(\tilde{U}^3 + \tilde{U} + \tilde{X})^{1/2}}. \quad (2.14a, b)$$

The curve $\tilde{Y} = \tilde{Y}_0(\tilde{X})$ defines a line of zero shear where the velocity \tilde{U} achieves a minimum; therefore, $\tau > 0$ for $\tilde{Y} > \tilde{Y}_0(\tilde{X})$, and $\tau < 0$ for $\tilde{Y} < \tilde{Y}_0(\tilde{X})$. It follows from equation (2.14b) that the curve $\tilde{Y}_0(\tilde{X})$ is the centreline about which the solution is symmetric; thus, the solution applies in the range $(0, 2\tilde{Y}_0(\tilde{X}))$. It is also evident from equation (2.13c) that the representation of u cannot be uniformly valid, and shear layers are required near the wall and far from the wall in order to adjust the drift velocity $-K$ to the no-slip condition and to the mainstream velocity, respectively; this structure is shown schematically in figure 1. Consequently, from equation (2.13c) it is evident that \tilde{U} must become large with the approach to the shear layers as $\tilde{Y} \rightarrow 0$ and $\tilde{Y} \rightarrow 2\tilde{Y}_0(\tilde{X})$ in order to overcome the small factor $(t_s - t)^{1/2}$ and thereby significantly alter the drift velocity $-K$. Because $\tilde{U} \rightarrow \infty$ as $\tilde{Y} \rightarrow 0$ and $\tilde{Y} \rightarrow 2\tilde{Y}_0(\tilde{X})$, in both cases equation (2.14b) gives

$$\tilde{Y}_0(\tilde{X}) = \int_{\tilde{U}_0}^{\infty} \frac{d\tilde{U}}{(\tilde{U}^3 + \tilde{U} + \tilde{X})^{1/2}}, \quad (2.15)$$

which is the equation of the central line; along this line the shear stress is zero, and it follows from equation (2.14a) that $\tilde{U}_0^3 + \tilde{U}_0 + \tilde{X} = 0$, which has one real solution given by

$$\tilde{U}_0(\tilde{X}) = \left[-\frac{\tilde{X}}{2} + \left(\frac{1}{27} + \frac{\tilde{X}^2}{4} \right)^{1/2} \right]^{1/3} + \left[-\frac{\tilde{X}}{2} - \left(\frac{1}{27} + \frac{\tilde{X}^2}{4} \right)^{1/2} \right]^{1/3}. \quad (2.16)$$

The terminal solution may be written in terms of elliptic integrals by introducing the transformation

$$\cos \theta = \frac{\tilde{U} - \tilde{U}_0 - \lambda^2}{\tilde{U} - \tilde{U}_0 + \lambda^2}, \quad \lambda^2 = (3\tilde{U}_0^2 + 1)^{1/2}. \quad (2.17a, b)$$

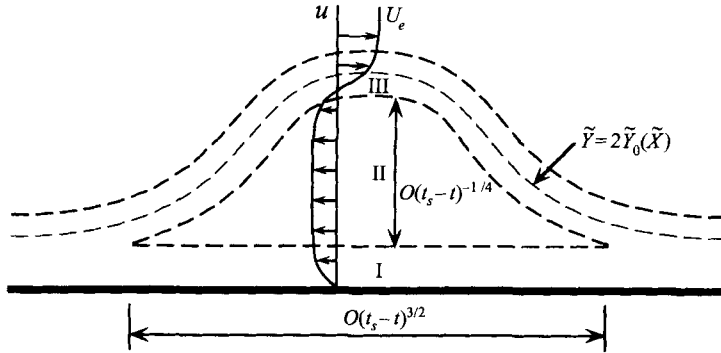


FIGURE 1. Schematic of the terminal boundary-layer structure near x_s (not to scale).

Substitution of equations (2.17) into the equation for the central line (2.15) gives

$$\tilde{Y}_0(\tilde{X}) = \frac{1}{\lambda} \int_0^\pi \frac{d\theta}{(1 - m \sin^2 \theta)^{1/2}} = \frac{2}{\lambda} F\left(\frac{1}{2}\pi | m \right) = \frac{2}{\lambda} K(m), \quad (2.18)$$

where F and K are incomplete and complete elliptic integrals of the first kind, respectively, with $m = \sin^2 \alpha = 1/2 - 3\tilde{U}_0/4\lambda^2$. Similarly, the equation for the velocity distribution (2.14b) becomes

$$\tilde{Y} - \tilde{Y}_0(\tilde{X}) = \frac{1}{\lambda} \int_\theta^\pi \frac{dz}{(1 - m \sin^2 z)^{1/2}} = \begin{cases} \tilde{Y}_0(\tilde{X}) - (1/\lambda)F(\theta|m), & 0 < \theta < \frac{1}{2}\pi \\ -(1/\lambda)F(\theta - \pi|m), & \frac{1}{2}\pi < \theta < \pi, \end{cases} \quad (2.19)$$

which along with equations (2.17) and (2.18) defines \tilde{U} as an implicit function of \tilde{Y} in a region bisected by the curve $\tilde{Y}_0(\tilde{X})$.

2.2. Properties of the terminal solution

The terminal solution describes the flow in the immediate vicinity of the separation point in a reference frame moving with the fluid particle which becomes longitudinally compressed to zero thickness as $t \rightarrow t_s$ (Van Dommelen 1981; Cowley *et al.* 1990). This particle is located within the boundary layer along the zero-vorticity line in accordance with the MRS conditions. The theoretical structure that occurs is illustrated in figure 1, where the streamwise scale of the eruptive zone has been greatly magnified for illustrative purposes. As shown the boundary layer bifurcates into two shear layers (regions I and III), above and below the central inviscid region (region II), as it evolves toward the eruptive state. A typical velocity profile is shown which indicates that the velocity is nearly constant across the central region in accordance with equation (2.13c) and then is adjusted across the upper and lower shear layers to the mainstream and wall velocities, respectively; region II is sometimes referred to as a vorticity-depleted or deadwater region. While the shear layers remain passive with thickness $O(Re^{-1/2})$ as $t \rightarrow t_s$, the deadwater zone contracts in the streamwise direction proportional to $(t_s - t)^{3/2}$ and expands proportional to $(t_s - t)^{-1/4}$ in the normal direction. Note that this structure is entirely contained within the initially thin boundary layer. As the singularity evolves, a spike forms in the displacement thickness, and although fluid particles in the upper part of the boundary layer will ultimately be located an infinite distance from the wall on the boundary-layer scale, this event on the physical scale appears as a small spike near the surface.

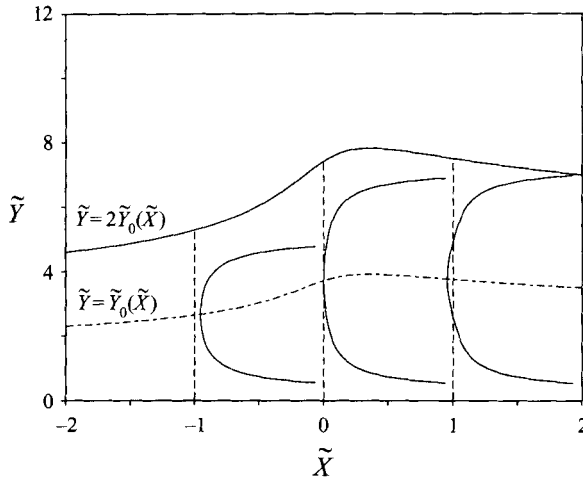


FIGURE 2. Velocity profiles for the terminal boundary-layer solution.

In this section the velocity distributions throughout the deadwater zone will be considered in more detail. The streamwise velocity profile at each fixed x may be found from a numerical solution of equation (2.19) using a procedure which will be discussed in §4, and some calculated profiles are shown in figure 2 which are representative of the flow in region II. Note that \tilde{U} becomes very large at the top and bottom of the domain in order to match to the shear layers in regions I and III, while near the central line $\tilde{Y}_0(\tilde{X})$, the velocity is positive for $\tilde{X} < 0$ and negative for $\tilde{X} > 0$. Therefore, the flow field near the centre of region II progressively focuses toward the point $(\tilde{X}, \tilde{Y}) = (0, \tilde{Y}_0(0))$, which is the eventual separation point; by continuity, the boundary layer must ultimately thicken near $\tilde{X} = 0$.

As $|\tilde{X}| \rightarrow \infty$, the asymptotic form of the streamwise velocity along the central line $\tilde{Y}_0(\tilde{X})$ follows from equation (2.16), and $\tilde{U}_0(\tilde{X}) \sim -\tilde{X}^{1/3}$ as $|\tilde{X}| \rightarrow \infty$. Consequently, \tilde{U} becomes very large in order to overcome the small factor $(t_s - t)^{1/2}$ in the transformation (2.13c) and adjust u from $-K$ to match a conventional boundary layer upstream and downstream of the eruptive zone. Therefore, at upstream and downstream infinity \tilde{U} may be neglected in (2.14b) compared to \tilde{U}^3 to leading order, and a similarity solution is easily found having the form $\tilde{U} = \bar{U}(\eta)|\tilde{X}|^{1/3}$, where $\eta = \tilde{Y}|\tilde{X}|^{1/6}$. The profile function \bar{U} may be found from equation (2.14b) and satisfies

$$\eta - \eta_0 = \begin{cases} \eta_0 - 3^{-1/4}F(\theta^*|m^*), & 0 < \theta^* < \frac{1}{2}\pi \\ -3^{-1/4}F(\theta^* - \pi|m^*), & \frac{1}{2}\pi < \theta^* < \pi, \end{cases} \quad (2.20)$$

where θ^* and η_0 are defined by

$$\cos \theta^* = \frac{\bar{U}(\eta) + b - 3^{1/2}}{\bar{U}(\eta) + b + 3^{1/2}}, \quad \eta_0 = \frac{2}{3^{1/4}}K(m^*), \quad (2.21a, b)$$

and the constants m^* and b are given by $m^* = \sin^2(\pi/12), b = -1$ for $\tilde{X} \rightarrow -\infty$ and $m^* = \sin^2(5\pi/12), b = 1$ for $\tilde{X} \rightarrow \infty$.

The form of the velocity at the vertical boundaries of region II as $\tilde{Y} \rightarrow 0$ and $\tilde{Y} \rightarrow 2\tilde{Y}_0(\tilde{X})$ is also of interest. From equations (2.14b) and (2.15) the solution above

and below the central line may be written

$$2\tilde{Y}_0 - \tilde{Y} = \int_{\tilde{U}}^{\infty} \frac{d\tilde{U}}{(\tilde{U}^3 + \tilde{U} + \tilde{X})^{1/2}}, \quad \tilde{Y} > \tilde{Y}_0(\tilde{X}), \quad (2.22a)$$

$$\tilde{Y} = \int_{\tilde{U}}^{\infty} \frac{d\tilde{U}}{(\tilde{U}^3 + \tilde{U} + \tilde{X})^{1/2}}, \quad \tilde{Y} < \tilde{Y}_0(\tilde{X}), \quad (2.22b)$$

respectively. Since $\tilde{U} \rightarrow \infty$ as $\tilde{Y} \rightarrow 0$, $2\tilde{Y}_0(\tilde{X})$, the integrands in equations (2.22) are, therefore, proportional to $\tilde{U}^{-3/2}$, and it follows from integration that

$$\tilde{U} \sim \frac{4}{\tilde{Y}^2} \quad \text{as } \tilde{Y} \rightarrow 0, \quad \tilde{U} \sim \frac{4}{(\tilde{Y} - 2\tilde{Y}_0)^2} \quad \text{as } \tilde{Y} \rightarrow 2\tilde{Y}_0(\tilde{X}). \quad (2.23a, b)$$

These are the matching conditions to the shear layers above and below region II and are also easily obtained from equation (2.19). Consequently, the central region II is characterized by unbounded streamwise velocities on all four sides.

Boundary-layer computations have been carried out up to the time of the terminal singularity using Lagrangian coordinates for a number of problems (Cowley *et al.* 1990); these include the impulsively started circular cylinder (Van Dommelen & Shen 1982), a vortex-induced boundary layer (Peridier *et al.* 1991a) and boundary-layer flow in a curved pipe (Lam 1988). In these cases a singularity was found to occur within a finite time which was generally characterized by the development of a sharp spike in the displacement thickness. The numerical results for times just prior to $t = t_s$ corroborate the asymptotic structure just described showing the evolution of a zero-vorticity line and a concentration of constant-vorticity contours representing the upper shear layer (region III). Velocity profiles near the eventual streamwise location of separation also reveal upper and lower shear layers surrounding the vorticity-depleted region where the velocity is nearly constant; a minimum in the velocity is also evident within the deadwater zone. In addition to these qualitative features, Peridier *et al.* (1991a) used a least-squares curve fit to determine the growth rate of the maximum in displacement thickness just prior to the singular time and found the growth rate to be $N = 0.253 \pm 0.003$; this is in good agreement with the theoretical value $N = 1/4$. The fact that a number of different problems evolve towards the same boundary-layer state supports the expectation that the terminal boundary-layer structure described here is generic and is independent of the pressure gradient which originally initiated the unsteady separation process.

3. The 'first' interactive stage

3.1. Eulerian formulation

The terminal solution describes the onset of a localized boundary-layer eruption that is characterized by a rapid growth in displacement thickness along a band in the streamwise direction which progressively narrows as $t \rightarrow t_s$. The formation of the singularity indicates that the initial non-interactive phase is breaking down as a significant interaction with the external flow starts to occur. Thus, a new subset of the Navier–Stokes equations must be used to reformulate the problem in the vicinity of the developing interaction just prior to $t = t_s$. Recall that as $t \rightarrow t_s$, the convective terms in the boundary-layer equations are $O[(t_s - t)^{-1/2}]$ and dominate both the pressure gradient and viscous terms. The so-called first interactive stage begins when the convective terms and pressure gradient become of comparable magnitude. Just

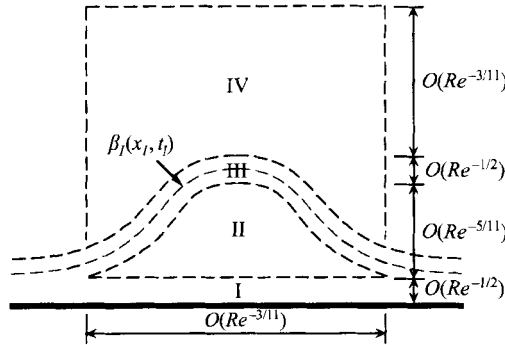


FIGURE 3. Schematic of the ‘first’ interactive stage of unsteady boundary-layer separation.

prior to this interaction, the boundary-layer thickness is $O(\delta)$ everywhere, where $\delta = Re^{-1/2}$, and as discussed in Appendix B, the pressure perturbations induced in the external flow are $O(Re^{-1/2})$. An expression for the induced pressure gradient perturbation is given in equation (B 4); since the streamwise extent of the developing eruption is very narrow, the leading term for the pressure p_0 may be replaced by the constant local value, say p_s , and the mainstream velocity u_0 by its local value $u_s = U_e(x_s)$. It follows from equation (B 4) that the induced pressure gradient has $\partial p/\partial x = O(Re^{-1/2} \partial^2 \delta^* / \partial x^2, Re^{-1/2} \partial^2 \delta^* / \partial x \partial t)$. Referring to figure 1, it may readily be inferred that the dominant contribution to the displacement thickness is associated with the expanding central region and that $\delta^* = O[(t_s - t)^{-1/4} \tilde{Y}_0(\tilde{X})]$. It follows from equations (2.13) that $\partial p/\partial x = O[Re^{-1/2}(t_s - t)^{-13/4}]$. Consequently, a balance occurs with the $O[(t_s - t)^{-1/2}]$ convective terms when $(t_s - t) = O(Re^{-2/11})$; therefore, this interaction becomes significant only a very short time before the formation of the non-interactive separation singularity. Events occurring within this time scale are expected to evolve very rapidly in order to relieve the non-interactive singularity and until now have been believed to represent the ‘first’ interactive stage encountered.

During this stage the upper and lower shear layers remain essentially passive having a thickness $O(Re^{-1/2})$, while the pressure distribution induced by the interaction begins to alter the flow in the intermediate region II of figure 3 between the shear layers. It follows from equations (2.2) that the streamwise and normal extent of the interactive zone are $O(Re^{-3/11})$ and $O(Re^{-5/11})$, respectively, and using equations (2.3) the following new variables for the central region II in this interactive stage are suggested:

$$x - x_s = K(t_s - t) + Re^{-3/11} \phi_0^{1/2} \bar{x}_I, \quad y = Re^{-5/11} A \phi_0^{-1/4} \bar{Y}_I, \quad t - t_s = Re^{-2/11} \bar{t}_I, \tag{3.1a, b, c}$$

$$u = -K + Re^{-1/11} \phi_0^{1/2} \bar{u}_I(\bar{x}_I, \bar{Y}_I, \bar{t}_I), \quad p = p_s + Re^{-2/11} \phi_0 \bar{p}_I(\bar{x}_I, \bar{Y}_I, \bar{t}_I). \tag{3.1d, e}$$

Here, the factors ϕ_0 and A (associated with the terminal solution) are inserted for convenience to be consistent with the variables in the previous stage defined in equations (2.13), and p_s denotes the mainstream pressure evaluated as $x \rightarrow x_s$. It is easily shown (Elliott *et al.* 1983) that

$$\frac{\partial \bar{u}_I}{\partial \bar{t}_I} + \bar{u}_I \frac{\partial \bar{u}_I}{\partial \bar{x}_I} - \frac{\partial \bar{\psi}_I}{\partial \bar{x}_I} \frac{\partial \bar{u}_I}{\partial \bar{Y}_I} = -\frac{\partial \bar{p}_I}{\partial \bar{x}_I}, \quad \bar{u}_I = \frac{\partial \bar{\psi}_I}{\partial \bar{Y}_I}, \quad \frac{\partial \bar{p}_I}{\partial \bar{Y}_I} = 0, \tag{3.2a, b, c}$$

where $\bar{\psi}_I$ is a perturbation streamfunction. These equations govern the evolution of the flow in the thickening central region II between $\bar{Y}_I = 0$ and the upper shear layer

at $\bar{Y}_I = \bar{\beta}_I(\bar{x}_I, \bar{t}_I)$. Note that $\bar{\beta}_I$ is to be found as part of the solution of the current interactive stage and that the problem is nonlinear and inviscid.

The solution of equations (3.2) on the interactive time scale as $\bar{t}_I \rightarrow -\infty$ must match the terminal boundary-layer solution as $t \rightarrow t_s^-$. Relating the interactive variables defined by equations (3.1) with the variables (2.13) for the terminal solution yields the following:

$$\bar{x}_I = (-\bar{t}_I)^{3/2} \tilde{X}, \quad \bar{Y}_I = (-\bar{t}_I)^{-1/4} \tilde{Y}, \quad \bar{u}_I(\bar{x}_I, \bar{Y}_I, \bar{t}_I) = (-\bar{t}_I)^{1/2} \tilde{U}(\tilde{X}, \tilde{Y}). \quad (3.3a, b, c)$$

These equations serve to provide initial conditions for large negative \bar{t}_I . Note that for fixed values of \tilde{X} and \tilde{Y} , \bar{x}_I increases and \bar{Y}_I decreases as $\bar{t}_I \rightarrow -\infty$ indicating that region II broadens in the streamwise direction and shrinks in the normal direction as time is decreased. Likewise, the perturbation velocity \bar{u}_I increases as $\bar{t}_I \rightarrow -\infty$ (relative to \tilde{U}) except as $|\tilde{X}|$ or $|\tilde{Y}| \rightarrow \infty$, where the steady similarity solutions exist. As $\bar{t}_I \rightarrow -\infty$, the initial condition for the equation of the upper shear layer is given by $\bar{Y}_I = \bar{\beta}_I(\bar{x}_I, \bar{t}_I) = (-\bar{t}_I)^{-1/4} 2\tilde{Y}_0(\tilde{X})$, and the matching conditions to the upper and lower shear layers (regions I and III, respectively, in figure 3), given in equations (2.23), become $\bar{u}_I \sim 4/\bar{Y}_I^2$ as $\bar{Y}_I \rightarrow 0$ and $\bar{u}_I \sim 4/(\bar{Y}_I - \bar{\beta}_I)^2$ as $\bar{Y}_I \rightarrow \bar{\beta}_I$. Because the perturbation velocities are very large near the upper and lower shear layers, an effective numerical solution method for equations (3.2) poses a formidable challenge.

To complete the formulation, it is necessary to evaluate the streamwise pressure gradient impressed by the outer inviscid flow due to the interactive effects. It is evident from equations (3.1a) and (3.1b) that the slope of the upper shear layer $\bar{Y}_I = \bar{\beta}_I$ is $O(Re^{-2/11})$; consequently, perturbations $O(Re^{-2/11})$ in the pressure and normal velocity are induced in a local interaction region IV (shown in figure 3) having dimensions $O(Re^{-3/11})$ by $O(Re^{-3/11})$. The solution in region IV leads to the pressure-displacement relation

$$\bar{p}_I(\bar{x}_I, \bar{t}_I) = -\frac{1}{\pi} \int_{-\infty}^{\infty} \frac{\partial \bar{\beta}_I(s, \bar{t}_I)}{\partial s} \frac{ds}{\bar{x}_I - s}, \quad (3.4)$$

which is derived in Appendix B. The growing region II leads to an increase in $\bar{\beta}_I$ which in turn influences the pressure and hence the flow in region II.

In principle, a numerical solution of the system (3.2) could be initiated at some large negative time t_{I0} using equations (3.3) to set the initial conditions. However, it is convenient to work in terms of the following scaled variables:

$$\bar{x}_I = (-t_{I0})^{3/2} x_I, \quad \bar{Y}_I = (-t_{I0})^{-1/4} Y_I, \quad \bar{t}_I = (-t_{I0}) t_I, \quad (3.5a, b, c)$$

$$\bar{u}_I = (-t_{I0})^{1/2} u_I, \quad \bar{p}_I = (-t_{I0}) p_I, \quad (3.5d, e)$$

for which equations (3.2) remain

$$\frac{\partial u_I}{\partial t_I} + u_I \frac{\partial u_I}{\partial x_I} - \frac{\partial \psi_I}{\partial x_I} \frac{\partial u_I}{\partial Y_I} = -\frac{\partial p_I}{\partial x_I}, \quad u_I = \frac{\partial \psi_I}{\partial Y_I}, \quad \frac{\partial p_I}{\partial Y_I} = 0, \quad (3.6a, b, c)$$

with the conditions at the upper and lower shear layers being

$$u_I \sim \frac{4}{Y_I^2} \quad \text{as } Y_I \rightarrow 0, \quad u_I \sim \frac{4}{(Y_I - \beta_I)^2} \quad \text{as } Y_I \rightarrow \beta_I. \quad (3.7a, b)$$

From equations (3.3) the initial condition at $t_I = -1$ is the terminal solution with

$$x_I = \tilde{X}, \quad Y_I = \tilde{Y}, \quad u_I(x_I, Y_I) = \tilde{U}(\tilde{X}, \tilde{Y}), \quad \beta_I(x_I) = \beta_0(x_I) = 2\tilde{Y}_0(\tilde{X}). \quad (3.8)$$

The starting time t_{I0} for the integrations appears in this formulation only in the

pressure-displacement relation (3.4) which becomes

$$p_I(x_I, t_I) = -\frac{(-t_{I0})^{-11/4}}{\pi} \int_{-\infty}^{\infty} \frac{\partial \beta_I(s, t_I)}{\partial s} \frac{ds}{x_I - s}. \quad (3.9)$$

In principle, solutions should be obtained for a range of values t_{I0} which are large and negative; evidently, the slope of the upper shear layer must grow significantly in order to overcome the small factor $(-t_{I0})^{-11/4}$ so that the perturbation pressure p_I becomes significant.

3.2. Lagrangian formulation

Because of the large perturbation velocities indicated by equations (3.7) near the top and bottom of region II as well as the fact that a focusing of the solution in the streamwise direction may occur, a solution of the system (3.6)–(3.9) does not appear to be feasible in the conventional Eulerian formulation. Thus, a Lagrangian formulation was adopted wherein the fluid particle positions (x_I, Y_I) and their corresponding velocity components (u_I, v_I) are evaluated as functions of their initial locations (ξ, η) and time t_I . In Lagrangian coordinates the analogue of equation (3.6a) governing the flow in region II is

$$\frac{\partial u_I}{\partial t_I} = -\frac{\partial p_I}{\partial x_I}, \quad \frac{\partial x_I}{\partial t_I} = u_I. \quad (3.10a, b)$$

The initial conditions specify the initial particle locations, with velocities given from the terminal solution (3.8), according to

$$x_I = \xi, \quad Y_I = \eta, \quad u_I = \tilde{U}(\xi, \eta) \quad \text{at} \quad t_I = -1. \quad (3.11)$$

The matching conditions (3.7) indicate that the motion must become plane parallel as the bounding shear layers of region II are approached; therefore, in these regions $Y_I = \eta$ for all t_I with

$$u_I \sim \frac{4}{\eta^2} \quad \text{as} \quad \eta \rightarrow 0, \quad u_I \sim \frac{4}{[\eta - \beta_0(\xi)]^2} \quad \text{as} \quad \eta \rightarrow \beta_0(\xi), \quad (3.12a, b)$$

where $\beta_0(\xi) = 2\tilde{Y}_0(\xi)$ defines the initial height of the upper shear layer in terms of the terminal solution.

In order to calculate the particle positions $x_I(\xi, \eta, t_I)$ and their velocities $u_I(\xi, \eta, t_I)$ from equations (3.10), the pressure must be evaluated from the interaction condition (3.9). This requires a knowledge of the location of the upper shear layer $\beta_I(x_I, t_I)$, and at any time t_I this is found from a solution of the continuity equation, which in Lagrangian coordinates is (see, for example, Van Dommelen & Shen 1980, 1982)

$$-\frac{\partial x_I}{\partial \eta} \frac{\partial Y_I}{\partial \xi} + \frac{\partial x_I}{\partial \xi} \frac{\partial Y_I}{\partial \eta} = 1. \quad (3.13)$$

For known streamwise particle positions $x_I(\xi, \eta, t_I)$, this is a first-order linear equation for the normal particle positions $Y_I(\xi, \eta, t_I)$ having the characteristics

$$\frac{d\xi}{-\partial x_I / \partial \eta} = \frac{d\eta}{\partial x_I / \partial \xi} = dY_I. \quad (3.14)$$

Each characteristic is a curve of constant x_I which represents the initial positions of a set of fluid particles that are currently located along the vertical line $x_I = \text{constant}$ at t_I . The values of Y_I at t_I , for particles which initially were distributed along the line $Y_I = \eta = \beta_0(\xi)$ at $t_I = -1$, defines the current height of region II, i.e. $Y_I = \beta_I(x_I, t_I)$, and permits the evaluation of pressure from the interaction condition (3.9).

The large velocities indicated by equations (3.12) at the edges of region II make the numerical solution of the problem as presently formulated problematic, and instead a velocity perturbation U_I about the terminal-solution velocity defined by

$$u_I(\xi, \eta, t_I) = \tilde{U}(\xi, \eta) + U_I(\xi, \eta, t_I) \quad (3.15)$$

was evaluated. The perturbation function U_I vanishes at $t_I = -1$ for all (ξ, η) , and integration of equation (3.10b) gives

$$x_I(\xi, \eta, t_I) = (t_I + 1)\tilde{U}(\xi, \eta) + X_I(\xi, \eta, t_I), \quad (3.16)$$

where X_I denotes the streamwise particle position perturbation. Thus to satisfy the initial conditions (3.11)

$$X_I(\xi, \eta, t_I) = \xi, \quad U_I(\xi, \eta, t_I) = 0 \quad \text{at } t_I = -1. \quad (3.17a, b)$$

Substitution of equations (3.15) and (3.16) into (3.10) gives

$$\frac{\partial U_I}{\partial t_I} = -\frac{\partial p_I}{\partial x_I}, \quad \frac{\partial X_I}{\partial t_I} = U_I, \quad (3.18a, b)$$

and thus the momentum equation for the perturbation quantities does not contain the terminal velocity distribution explicitly. Note that \tilde{U} identically satisfies the unbounded velocity conditions (3.12) at the edges of region II, where the perturbation function U_I is, therefore, bounded and independent of η . Substitution of equation (3.16) into (3.13) gives

$$- \left[(t_I + 1) \frac{\partial \tilde{U}}{\partial \eta} + \frac{\partial X_I}{\partial \eta} \right] \frac{\partial Y_I}{\partial \xi} + \left[(t_I + 1) \frac{\partial \tilde{U}}{\partial \xi} + \frac{\partial X_I}{\partial \xi} \right] \frac{\partial Y_I}{\partial \eta} = 1 \quad (3.19)$$

for the continuity equation. It is evident that interaction affects the computation of the characteristics of equation (3.19) through the particle position perturbation $X_I(\xi, \eta, t_I)$, while the remaining coefficients are associated with the terminal solution. Since the terminal velocity $\tilde{U}(\xi, \eta)$ is symmetric about the central line $\eta = \beta_0(\xi)/2 = \tilde{Y}_0(\xi)$ that bisects the intermediate region II, the coefficient of $\partial Y_I/\partial \xi$ in equation (3.19) is anti-symmetric about this line; on the other hand, the coefficient of $\partial Y_I/\partial \eta$ is symmetric about the central curve. As a result, all characteristics are symmetric about $\eta = \beta_0(\xi)/2 = \tilde{Y}_0(\xi)$ for all t_I .

It follows from equations (3.14) that the vertical position of a fluid particle initially located at (ξ, η) is given by

$$Y_I(\xi, \eta, t_I) - Y_{I0} = \int_{(\xi_0, \eta_0)}^{(\xi, \eta)} \frac{ds}{[(\partial x_I/\partial \xi)^2 + (\partial x_I/\partial \eta)^2]^{1/2}}, \quad (3.20)$$

where the integral is along the constant x_I characteristic passing through the point (ξ, η) and originating at (ξ_0, η_0) where $Y_I = Y_{I0}$. A singularity occurs when a particle at an initial position (ξ, η) is eventually located at an infinite normal distance from the surface, and from equation (3.20) this occurs when a stationary point develops in the x_I field at some location (ξ_s, η_s) at time t_{Is} , viz.

$$\frac{\partial x_I}{\partial \xi} = \frac{\partial x_I}{\partial \eta} = 0 \quad \text{at } \xi = \xi_s, \eta = \eta_s, t_I = t_{Is}. \quad (3.21)$$

In the present case, the coefficient of $\partial Y_I/\partial \xi$ in equation (3.19) is zero (for all t_I) along the central line (which defines the zero-vorticity line $\partial u_I/\partial Y_I = 0$) due to symmetry of the flow. If a singularity occurs, therefore, it must develop when the

coefficient of $\partial Y_I / \partial \eta$ in equation (3.19) becomes zero at some point along the central line $\eta = \beta_0(\xi)/2$, viz.

$$(t_I + 1) \frac{\partial \tilde{U}}{\partial \xi} + \frac{\partial X_I}{\partial \xi} = 0, \quad (3.22)$$

at some ξ_s , where $\eta_s = \beta_0(\xi_s)/2$. Note that this coefficient is unity everywhere at the start of the integration at $t_I = -1$.

3.3. Finite-domain transformation

To obtain a numerical solution, it is convenient to transform region II into a finite rectangular domain. The streamwise coordinate, particle position and particle position perturbation are defined on the range $(-\infty, \infty)$ and can be transformed to the finite range $(-1, 1)$ by

$$\hat{\xi} = \frac{2}{\pi} \arctan\left(\frac{\xi}{a}\right), \quad \hat{x}_I = \frac{2}{\pi} \arctan\left(\frac{x_I}{a}\right), \quad \hat{X}_I = \frac{2}{\pi} \arctan\left(\frac{X_I}{a}\right), \quad (3.23a, b, c)$$

respectively. Here, a is a stretching parameter that affects the concentration of points near $\xi = 0$; for a uniform mesh in $\hat{\xi}$, a relatively larger number of mesh points are clustered near $\xi = 0$ for smaller values of a . The normal coordinate is defined in the range $(0, \beta_0(\hat{\xi}))$ in region II, and it is convenient to apply the scaling $\hat{\eta} = 2\eta/\beta_0(\hat{\xi})$, so that the lower and upper shear layers are at $\hat{\eta} = 0, 2$, respectively, and $\hat{\eta} = 1$ corresponds to the central line. The momentum equation (3.18) and continuity equation (3.19) become

$$\begin{aligned} \frac{\partial U_I}{\partial t_I} &= -\frac{\Gamma(\hat{x}_I)}{a} \frac{\partial p_I}{\partial \hat{x}_I}, \quad \frac{\partial \hat{X}_I}{\partial t_I} = \frac{\Gamma(\hat{X}_I)}{a} U_I, \quad (3.24a, b) \\ - \left[(t_I + 1) \frac{\partial \tilde{U}}{\partial \hat{\eta}} + \frac{a}{\Gamma(\hat{X}_I)} \frac{\partial \hat{X}_I}{\partial \hat{\eta}} \right] \frac{\partial Y_I}{\partial \hat{\xi}} + \left[(t_I + 1) \frac{\partial \tilde{U}}{\partial \hat{\xi}} + \frac{a}{\Gamma(\hat{X}_I)} \frac{\partial \hat{X}_I}{\partial \hat{\xi}} \right] \frac{\partial Y_I}{\partial \hat{\eta}} &= \frac{a \beta_0(\hat{\xi})}{2 \Gamma(\hat{\xi})}. \end{aligned} \quad (3.25)$$

where $\Gamma(z) = [1 + \cos(\pi z)]/\pi$. The initial conditions (3.11) are now

$$\hat{X}_I = \hat{\xi}, \quad Y_I = \frac{\beta_0(\hat{\xi})}{2} \hat{\eta}, \quad U_I(\hat{\xi}, t_I) = 0 \quad \text{at } t_I = -1, \quad (3.26)$$

while the conditions (3.12) to match to the shear layers above and below region II are

$$u_I \sim \frac{16}{\beta_0^2(\hat{\xi}) \hat{\eta}^2} \quad \text{as } \hat{\eta} \rightarrow 0, \quad u_I \sim \frac{16}{\beta_0^2(\hat{\xi}) (\hat{\eta} - 2)^2} \quad \text{as } \hat{\eta} \rightarrow 2. \quad (3.27a, b)$$

4. Numerical methods

The general procedure in a numerical solution at each time step is as follows. The solution of equations (3.24) provides the velocity perturbation $U_I(\hat{\xi}, \hat{\eta}, t_I)$ and particle position perturbation $\hat{X}_I(\hat{\xi}, \hat{\eta}, t_I)$ at each time step for a given estimate of the pressure gradient. The distribution $\hat{X}_I(\hat{\xi}, \hat{\eta}, t_I)$ is necessary, along with the terminal-state velocity $\tilde{U}(\hat{\xi}, \hat{\eta})$, in order to solve the continuity equation (3.25) for the normal particle positions $Y_I(\hat{\xi}, \hat{\eta}, t_I)$ and the upper boundary $\beta_I(\hat{x}_I, t_I)$ of region II. The Cauchy integral (3.9) of $\partial \beta_I / \partial x_I$ then gives a new iterate for the pressure

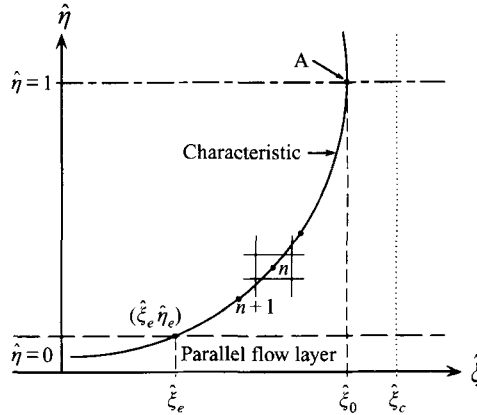


FIGURE 4. Schematic of integration along a characteristic $\hat{x}_I = \text{constant}$ at time t_I : ———, characteristic $\hat{x}_I = \hat{\xi}_c$; ·····, current location of fluid particles at time t_I which originated at $t_I = -1$ on the characteristic curve.

distribution $p_I(\hat{x}_I, t_I)$. Unlike the noninteractive case, the solutions of the momentum and continuity equations are strongly coupled.

Integration of the momentum equations (3.24) and the continuity equation (3.25) is accomplished on a two-dimensional mesh which must be defined in the $\hat{\xi}$ - and $\hat{\eta}$ -directions. However, the position of the upper shear layer may be calculated from the continuity equation for any desired $\hat{\xi}$ -location, and in principle, the mesh for $U_I(\hat{\xi}, \hat{\eta}, t_I)$, $\hat{X}_I(\hat{\xi}, \hat{\eta}, t_I)$, $p_I(\hat{x}_I, t_I)$ and $\beta_I(\hat{x}_I, t_I)$ may be defined independently of the two-dimensional mesh associated with the continuity equation. Although this approach was tried, it is generally not advantageous because the dependent variables are highly interdependent and basically require the same degree of resolution. Recall that the solution of the momentum equations and the characteristics of the continuity equation are symmetric about the central line $\hat{\eta} = 1$. Therefore, the two-dimensional mesh associated with each need only be defined over the lower half of the domain, i.e. for $-1 \leq \hat{\xi} \leq 1$ and $0 \leq \hat{\eta} \leq 1$. The $\hat{\xi}$ - and $\hat{\eta}$ -intervals were subdivided into a total of $I_0 - 1$ and $J_0 - 1$ equal subintervals, respectively, with the mesh locations $(\hat{\xi}_i, \hat{\eta}_j)$ defined for $i = 1, \dots, I_0$ and $j = 1, \dots, J_0$. The streamwise interval for the one-dimensional functions $p_I(\hat{x}_I, t_I)$ and $\beta_I(\hat{x}_I, t_I)$ was subdivided into a total of $I_0 - 1$ equal subintervals.

4.1. Momentum equation

In order to integrate the inviscid momentum equations (3.24) forward in time, a predictor-corrector method was used. Denote the time step by Δt_I and the known pressure gradient at \hat{x}_I from the previous time step by $(\partial p_I / \partial \hat{x}_I)_i^*$; here and throughout, an asterisk denotes a known quantity at $t_I^* = t_I - \Delta t_I$. Predicted values of $U_{Ip}(\hat{\xi}_i, \hat{\eta}_j, t_I)$ and $\hat{X}_I(\hat{\xi}_i, \hat{\eta}_j, t_I)$ were estimated using the following first-order (in Δt_I) difference formulae:

$$U_{Ip}(\hat{\xi}_i, \hat{\eta}_j, t_I) = U_{Ip}(\hat{\xi}_i, \hat{\eta}_j, t_I^*) - \frac{\Gamma[\hat{x}_I(\hat{\xi}_i, \hat{\eta}_j, t_I^*)]}{a} \left(\frac{\partial p_I}{\partial \hat{x}_I} \right)_i^* \Delta t_I, \quad (4.1a)$$

$$\hat{X}_{Ip}(\hat{\xi}_i, \hat{\eta}_j, t_I) = \hat{X}_I(\hat{\xi}_i, \hat{\eta}_j, t_I^*) + \frac{\Gamma[\hat{X}_I(\hat{\xi}_i, \hat{\eta}_j, t_I^*)]}{a} U_{Ip}(\hat{\xi}_i, \hat{\eta}_j, t_I) \Delta t_I, \quad (4.1b)$$

for $i = 1, \dots, I_0$, $j = 1, \dots, J_0$. With these estimates for $U_{I_p}(\hat{\xi}_i, \hat{\eta}_j, t_l)$ and $\hat{X}_{I_p}(\hat{\xi}_i, \hat{\eta}_j, t_l)$, the pressure gradient $(\partial p_I / \partial \hat{x}_I)_i$ was estimated at the current time step using an algorithm that will be described in §4.3. The distributions of $U_I(\hat{\xi}_i, \hat{\eta}_j, t_l)$ and $\hat{X}_I(\hat{\xi}_i, \hat{\eta}_j, t_l)$ at the current time step were then refined using the following second-order accurate formulae:

$$U_I(\hat{\xi}_i, \hat{\eta}_j, t_l) = U_I(\hat{\xi}_i, \hat{\eta}_j, t_l^*) - \frac{\Gamma[\hat{x}_I(\hat{\xi}_i, \hat{\eta}_j, t_l^*)] (\partial p_I / \partial \hat{x}_I)_i^* + \Gamma[\hat{x}_{I_p}(\hat{\xi}_i, \hat{\eta}_j, t_l)] (\partial p_I / \partial \hat{x}_I)_i}{2a} \Delta t_l, \quad (4.2a)$$

$$\hat{X}_I(\hat{\xi}_i, \hat{\eta}_j, t_l) = \hat{X}_I(\hat{\xi}_i, \hat{\eta}_j, t_l^*) + \frac{\Gamma[\hat{X}_I(\hat{\xi}_i, \hat{\eta}_j, t_l^*)] U_{I_p}(\hat{\xi}_i, \hat{\eta}_j, t_l) + \Gamma[\hat{X}_{I_p}(\hat{\xi}_i, \hat{\eta}_j, t_l)] U_I(\hat{\xi}_i, \hat{\eta}_j, t_l)}{2a} \Delta t_l, \quad (4.2b)$$

for $i = 1, \dots, I_0$, $j = 1, \dots, J_0$. Observe that in equations (4.1a) and (4.2a), the pressure gradient must be evaluated at the current particle position location \hat{x}_I whose value may be obtained from equations (3.16) and (3.23). Therefore, to determine $(\partial p_I / \partial \hat{x}_I)_i$ the pressure gradient was evaluated using central differences at mesh locations $\hat{\xi}_i$, $i = 1, \dots, I_0$, and values of $\partial p_I / \partial \hat{x}_I$ were interpolated, as needed, using linear interpolation. The pressure distribution at the current time was obtained through a calculation along the characteristics of the continuity equation to find the current equation of the upper shear layer $\beta_I(\hat{\xi}_i, t_l)$ which is needed in the interaction condition defining the pressure distribution. The methods for these two steps are discussed next.

4.2. Equation of the upper shear layer

Inspection of the continuity equation (3.25) reveals that the influence of interaction is represented by the particle position perturbation $\hat{X}_I(\hat{\xi}_i, \hat{\eta}_j, t_l)$, with the remainder of the terms consisting of the terminal solution. To evaluate the terminal-state velocity distribution $\tilde{U}(\hat{\xi}, \hat{\eta})$ and the initial displacement thickness $\beta_0(\hat{\xi}) = 2\tilde{Y}_0(\hat{\xi})$, the necessary complete and incomplete elliptic integrals were calculated using the descending Landen transformation described in Abramowitz & Stegun (1964). To compute the terminal-state velocity distribution $\tilde{U}(\hat{\xi}_i, \hat{\eta}_j)$ on the computational mesh, an implicit procedure was required. For a given point in the mesh $(\hat{\xi}_i, \hat{\eta}_j)$, the central line velocity $\tilde{U}_0(\hat{\xi}_i)$ was determined using equation (2.16), and λ was obtained from equation (2.17b). For a specified value of $\tilde{Y} = \eta$, the value of θ was found using a root finding technique such that equation (2.19) was satisfied; $\tilde{U}(\hat{\xi}_i, \hat{\eta}_j)$ was subsequently determined from equation (2.17a). In this manner $\tilde{U}(\hat{\xi}_i, \hat{\eta}_j)$ was evaluated on a two-dimensional mesh defined for $i = 1, \dots, I_0$, $j = 1, \dots, J_0$.

For known distributions of \hat{X} and \tilde{U} , the continuity equation in Lagrangian coordinates is a first-order linear equation which is of the form

$$P(\hat{\xi}, \hat{\eta}, t_l) \frac{\partial Y_I}{\partial \hat{\xi}} + Q(\hat{\xi}, \hat{\eta}, t_l) \frac{\partial Y_I}{\partial \hat{\eta}} = R(\hat{\xi}, \hat{\eta}, t_l), \quad (4.3)$$

where the coefficients are

$$P = -(t_l + 1) \frac{\partial \tilde{U}}{\partial \hat{\eta}} - \frac{a}{\Gamma(\hat{X}_I)} \frac{\partial \hat{X}_I}{\partial \hat{\eta}}, \quad Q = (t_l + 1) \frac{\partial \tilde{U}}{\partial \hat{\xi}} + \frac{a}{\Gamma(\hat{X}_I)} \frac{\partial \hat{X}_I}{\partial \hat{\xi}}, \quad R = \frac{a \beta_0(\hat{\xi})}{2 \Gamma(\hat{\xi})}. \quad (4.4a, b, c)$$

Note that the coefficient $R = R(\hat{\xi})$, and the partial derivatives of \tilde{U} in equations (4.4a) and (4.4b) do not change with time and were, therefore, evaluated once and for all using central differences. The partial derivatives of \hat{X}_I in equations (4.4a) and (4.4b) were calculated during the course of the integration, also using central differences.

The numerical solution of equation (4.3) was obtained by integration along characteristics which have the equations $d\hat{\xi}/P = d\hat{\eta}/Q = dY_I/R = ds$, where s is a variable measured along a characteristic. The integration can be carried out to determine the normal position $Y_I(\hat{\xi}, \hat{\eta}, t_I)$ of any fluid particle, but the equation of the upper shear layer $\beta_I(\hat{\xi}, t_I) = Y_I(\hat{\xi}, 2, t_I)$ is of particular interest. In a conventional calculation (see, for example, Van Dommelen & Shen 1980, 1982), integration along the characteristics is initiated at the surface, where $x_I = \xi$ and $Y_I = 0$ for all time, since the no-slip condition requires that particles which are initially on the wall must remain there. In the present problem, the integration cannot be initiated at $\hat{\eta} = 0$ because of the large streamwise velocity condition (3.27a) as $\hat{\eta} \rightarrow 0$ and must, therefore, begin at a more convenient location. To this end, consider integration of $dY_I = R(\hat{\xi})ds$ along a characteristic. Since the right-hand side is independent of Y_I , it is not necessary to know the value of Y_I at $s = 0$, and the integration, in effect, produces the change in Y_I between any two points. In this study integrations were carried out starting from where the characteristics intersect the central line ($\hat{\eta} = 1$) and moving downward toward the plane-parallel flow layer that develops as $\hat{\eta} \rightarrow 0$, as illustrated schematically in figure 4. This is convenient because fluid particles which start on the central line at $t_I = -1$ must remain there with $\hat{\eta} = 1$. In order to initiate the integration along the characteristic and thereby compute the height of the upper shear layer at some point \hat{x}_I , it is necessary to determine where a fluid particle on the central line, which at time t_I is located at $\hat{x}_I = \hat{\xi}_c$ say, started out at time $t_I = -1$. Denote this initial position by $\hat{\xi}_0$, and for the illustrative situation shown in figure 4, the fluid particle at initial position A is now at $\hat{x}_I = \hat{\xi}_c$ and thus is assumed to have experienced a drift to the right along the central line in the time interval from $t_I = -1$ to the current value t_I . Therefore, from equations (3.16) and (3.23b), the value of $\hat{\xi}_0$ is determined from the relation

$$x_I(\hat{\xi}_0, 1, t_I) = (t_I + 1)\tilde{U}(\hat{\xi}_0, 1) + a \tan \left[\frac{1}{2}\pi \hat{X}_I(\hat{\xi}_0, 1, t_I) \right] = \hat{\xi}_c, \quad (4.5)$$

and for a given $\hat{x}_I = \hat{\xi}_c$ at time t_I , the appropriate value of $\hat{\xi}_0$ was evaluated iteratively using second-order-accurate interpolation formulae. Consequently, the initial conditions for integration along a characteristic are $\hat{\xi} = \hat{\xi}_0$, $\hat{\eta} = 1$ and $Y_I = 0$ at $s = 0$. The characteristics have the general shape indicated in figure 4 and bend to the left as they approach the lower shear layer. Because of the high velocities near the lower shear layer, all characteristics emanate from the lower left corner at $\hat{\xi} = -1$ and $\hat{\eta} = 0$. Similarly, all characteristics in the upper portion of the boundary layer bend to the left above $\hat{\eta} = 1$ and terminate in the upper left corner at $\hat{\xi} = -1$ and $\hat{\eta} = 2$.

Integration of the characteristic equations was carried out in the $(\hat{\xi}, \hat{\eta})$ -plane using a predictor-corrector algorithm to step along the characteristics. Assume that the integration along the characteristic has reached the n th point denoted by $(\hat{\xi}^n, \hat{\eta}^n)$ and $Y_I = Y_I^n$ and that the coordinates of the next point $(\hat{\xi}^{n+1}, \hat{\eta}^{n+1})$, where $Y_I = Y_I^{n+1}$, are to be evaluated next. First, the coefficients P^n , Q^n and R^n of the continuity equation at the n th point must be computed, and this was accomplished using bilinear interpolation between the four mesh points surrounding the point $(\hat{\xi}^n, \hat{\eta}^n)$ (see

Abramowitz & Stegun 1964). The length of the next step along the characteristic was evaluated from the following relation:

$$\Delta s = \frac{\theta \Delta \hat{\xi}}{[(P^n)^2 + (Q^n)^2]^{1/2}}, \quad (4.6)$$

where $0 < \theta \leq 1$, and a typical value of θ used was $\theta = 0.25$. This formula restricts the step along the characteristic so that the arc length involved is some fraction of the mesh spacing $\Delta \hat{\xi}$ and produces very small steps in s near $\hat{\eta} = 0$, where the coefficients P and Q become large. The location and normal distance of the $(n+1)$ point were then predicted using

$$\hat{\xi}_p^{n+1} = \hat{\xi}^n - P^n \Delta s, \quad \hat{\eta}_p^{n+1} = \hat{\eta}^n - Q^n \Delta s, \quad Y_{I_p}^{n+1} = Y_I^n + R^n \Delta s, \quad (4.7a, b, c)$$

where the negative signs in equations (4.7a,b) arise because the integration was carried out backward along the characteristic starting from the central line $\hat{\eta} = 1$ and moving toward the bottom shear layer at $\hat{\eta} = 0$. The coefficients P^{n+1} , Q^{n+1} and R^{n+1} were then evaluated at the point $(\hat{\xi}_p^{n+1}, \hat{\eta}_p^{n+1})$ through interpolation, and the corrector algorithm was implemented using

$$\hat{\xi}^{n+1} = \hat{\xi}^n - \frac{1}{2}(P^n + P^{n+1})\Delta s, \quad \hat{\eta}^{n+1} = \hat{\eta}^n - \frac{1}{2}(Q^n + Q^{n+1})\Delta s, \quad (4.8a, b)$$

$$Y_I^{n+1} = Y_I^n + \frac{1}{2}(R^n + R^{n+1})\Delta s. \quad (4.8c)$$

Each integration proceeds along the characteristic in this way until the vicinity of the parallel flow layer is reached as $\hat{\eta} \rightarrow 0$. The level at which the characteristic integration is terminated must be carefully chosen; it must be near enough to $\hat{\eta} = 0$ so that the flow is essentially plane parallel but still sufficiently large so that substantial computational errors do not arise from attempting to integrate too far through this high-velocity region where, as illustrated in figure 4, the characteristics continue far upstream gradually asymptoting to $\hat{\eta} = 0$. A typical value of η_e used in the present integrations was $\eta_e = 0.7$. Once the parallel flow region is reached, the contribution to the normal distance Y_I from the remainder of the characteristic is simply the initial normal coordinate η_e of the point, since $Y_I = \eta_e$ for locations in the parallel flow layer. Because region II is symmetric about the central line, the current distance of the upper shear layer from the wall at $\hat{x}_I = \hat{\xi}_c$ is given by

$$\beta_I(\hat{\xi}_c, t_I) = 2(Y_{I_e} + \eta_e). \quad (4.9)$$

Here, Y_{I_e} is the value of Y_I obtained in the integration along the characteristic from $\hat{\eta} = 1$ to $\hat{\eta} = \hat{\eta}_e$; in reality Y_{I_e} constitutes the change in Y_I from $\hat{\eta}_e$ to the central line. The characteristic integration was executed for each point in the mesh $\hat{\xi}_i$, where $i = 1, \dots, I_0$, to obtain the equation of the upper shear layer at the current time.

As a cross-check, the interpolation required in the above scheme at each point $(\hat{\xi}^n, \hat{\eta}^n)$ along a characteristic was replaced by a semi-analytical method of evaluating the coefficients P^n and Q^n in equations (4.4) as a test of the accuracy. The term $\partial \tilde{U} / \partial \hat{\eta}$ was evaluated at any point using equation (2.14a) with $\tilde{U}(\hat{\xi}^n, \hat{\eta}^n)$ being calculated directly from the terminal solution given in equations (2.16)–(2.19) rather than from interpolation. An analytical expression for $\partial \tilde{U} / \partial \hat{\xi}$ is difficult to obtain, but a very accurate evaluation is possible using a central-difference approximation if \tilde{U} is found (from the terminal solution) for points $(\hat{\xi}^n - \Delta \hat{\xi}, \hat{\eta}^n)$ and $(\hat{\xi}^n + \Delta \hat{\xi}, \hat{\eta}^n)$ with a very small value of $\Delta \hat{\xi}$. This alternative method for the determination of P^n and Q^n requires many evaluations of the streamwise velocity \tilde{U} at each time step and is, therefore,

very time consuming. Since the semi-analytical method produced essentially the same results at the small mesh sizes used in the present study, the more efficient interpolation method was used in the majority of the calculations.

4.3. Interaction condition

The interaction condition (3.9) relates the pressure to the growing distance of the upper shear layer from the wall and involves a Cauchy principal-value integral. An accurate numerical method to evaluate this integral is believed to be critical to the success of the overall scheme. The Cauchy integral on the right-hand side of equation (3.9) can be written in the form

$$C(x) = \frac{1}{\pi} \int_{-\infty}^{\infty} \frac{F(s)}{x-s} ds, \quad F(x) = -(-t_{I0})^{-11/4} \frac{\partial \beta_I(x)}{\partial x}. \quad (4.10a, b)$$

Here, the time dependence is omitted for convenience since the interaction condition is evaluated at fixed t_I ; in addition, the subscript I will be omitted from x in the remainder of this section. To calculate C at a typical point x_m in the mesh, the integral is divided into two parts $C(x_m) = S_m + L_m$, corresponding to the main part of the integral and the asymptotic tails defined by

$$S_m = \frac{1}{\pi} \int_{-R}^R \frac{F(s)}{x_m - s} ds, \quad L_m = \frac{1}{\pi} \left\{ \int_{-\infty}^{-R} \frac{F(s)}{x_m - s} ds + \int_R^{\infty} \frac{F(s)}{x_m - s} ds \right\}, \quad (4.11a, b)$$

respectively, where R is some large fixed value of x . Variables \hat{s} and \hat{x} were defined in the range $(-1, 1)$ by transformations similar to equations (3.23), and the interval was divided into M equal segments of length $\Delta \hat{x}$. The constant R was chosen so that the asymptotic tails are taken over the last half-intervals according to

$$R = a \tan \left\{ \frac{1}{2} \pi \left(1 - \frac{1}{2} \Delta \hat{x} \right) \right\}. \quad (4.12)$$

The main part (4.11a) of the Cauchy integral becomes

$$S_m = \frac{1}{2} \cos \left(\frac{1}{2} \pi \hat{x}_m \right) \int_{-\hat{R}}^{\hat{R}} \frac{H(\hat{s})}{\sin \left[\frac{1}{2} \pi (\hat{x}_m - \hat{s}) \right]} d\hat{s}, \quad H(\hat{x}) = \frac{F(\hat{x})}{\cos \left(\frac{1}{2} \pi \hat{x} \right)}, \quad (4.13a, b)$$

and a second-order-accurate approximation of the form

$$S_m = \frac{1}{2} \cos \left(\frac{1}{2} \pi \hat{x}_m \right) \sum_{n=2}^M \{ A_{mn} H_n + B_{mn} H'_n \}, \quad (4.14)$$

may be developed (Peridier *et al.* 1991b) by approximating $H(\hat{s})$ as varying linearly over each interval in the mesh; here, H'_n denotes the derivative of $H(\hat{x})$ at $\hat{x} = \hat{x}_n$. Expressions for the coefficients in equation (4.14) have been given by Peridier *et al.* (1991b) as

$$A_{mn} = -\frac{1}{\pi} \log \left\{ \frac{\sin r_{mn} - \sin \left(\frac{1}{2} \pi \epsilon \right)}{\sin r_{mn} + \sin \left(\frac{1}{2} \pi \epsilon \right)} \right\}^2, \quad (4.15a)$$

$$B_{mn} = \begin{cases} -\frac{(\Delta \hat{x})^2}{\pi \epsilon \cos r_{mn}} \left\{ 1 + \frac{\tan r_{mn}}{\pi \epsilon} \log \left| \frac{2 \sin r_{mn} - \pi \epsilon \cos r_{mn}}{2 \sin r_{mn} + \pi \epsilon \cos r_{mn}} \right| \right\}, & |r_{mn}| < 0.6 \\ \frac{1}{3} \pi \epsilon^3 \frac{\cos r_{mn}}{\sin^2 r_{mn}} + \dots, & |r_{mn}| > 0.6 \end{cases}, \quad (4.15b)$$

where $r_{mn} = \pi(\hat{x}_m - \hat{x}_n)/2$ and $\epsilon = \Delta\hat{x}/2$.

It is noted in passing that an analogue of this scheme for a non-uniform mesh in \hat{x} has been described in Cassel (1993) and was utilized in the present study with the view of enhancing resolution in local regions (particularly near $\hat{x} = 0$) where intense variations were found to ultimately occur in the solution. However, the method requires considerably more storage ($O(M^2)$), as apposed to $O(M)$ for the uniform mesh, as well as a substantial increase in computational time; therefore, it was judged that the increase in local accuracy was not sufficient to justify the substantial loss in computational efficiency with this method, and a uniform mesh in \hat{x} was used for the majority of the calculations.

Now consider the contribution of the asymptotic tails to the Cauchy integral. Substitution of equation (2.17b) with $\tilde{U}_0 \sim -\tilde{X}^{1/3}$ as $|\tilde{X}| \rightarrow \infty$ into (2.18) gives the following expressions for the distance to the upper shear layer at large x :

$$\beta_I \sim -\frac{4K\left(\frac{5}{12}\pi\right)}{3^{1/4}x^{1/6}} \quad \text{as } x \rightarrow \infty, \quad \beta_I \sim \frac{4K\left(\frac{1}{12}\pi\right)}{3^{1/4}(-x)^{1/6}} \quad \text{as } x \rightarrow -\infty, \quad (4.16a, b)$$

where K is the complete elliptic integral, and substitution in equation (4.11b) yields

$$L_m = \frac{2(-t_{I0})^{-11/4}}{3^{5/4}\pi} \left\{ K\left(\frac{1}{12}\pi\right) \int_{-\infty}^{-R} \frac{ds}{(-s)^{7/6}(s-x_m)} - K\left(\frac{5}{12}\pi\right) \int_R^{\infty} \frac{ds}{s^{7/6}(s-x_m)} \right\}. \quad (4.17)$$

Evaluation of the integrals gives

$$L_m = \begin{cases} \frac{1}{6} \frac{(-t_{I0})^{-11/4}}{3^{1/4}\pi|x_m|^{7/6}} \left\{ K\left(\frac{1}{12}\pi\right) T_-(x_m) - K\left(\frac{5}{12}\pi\right) T_+(x_m) \right\}, & x_m \neq 0 \\ -\frac{4}{7} \frac{(-t_{I0})^{-11/4}}{3^{1/4}\pi R^{7/6}} \left\{ K\left(\frac{1}{12}\pi\right) + K\left(\frac{5}{12}\pi\right) \right\}, & x_m = 0 \end{cases}. \quad (4.18)$$

Here, $(T_-, T_+) = (-T_1, T_2)$ for $x_m > 0$, and $(T_-, T_+) = (T_2, -T_1)$ for $x_m < 0$, where

$$T_1(x_m) = 24\gamma - \sqrt{3} \log \left\{ \frac{\gamma^2 + \sqrt{3}\gamma + 1}{\gamma^2 - \sqrt{3}\gamma + 1} \right\}^2 - 8 \tan^{-1} \gamma - 4 \tan^{-1} \left\{ \frac{\gamma}{1-\gamma^2} \right\}, \quad (4.19a)$$

$$T_2(x_m) = 24\gamma + \log \left\{ \frac{(1+\gamma^3)(1-\gamma)^3}{(1-\gamma^3)(1+\gamma)^3} \right\}^2 - 4\sqrt{3} \tan^{-1} \left\{ \frac{\sqrt{3}\gamma}{1-\gamma^2} \right\}, \quad (4.19b)$$

with $\gamma = |x_m/R|^{1/6}$.

5. Calculated results

As a test of the algorithm described in §4, a set of calculations were carried out with the pressure gradient set equal to zero in equation (3.18a); the numerical solution should then consist of the continuation of the known exact terminal solution which ultimately must become singular at $t_I = 0$. The ability of the numerical algorithm to continue to track the solution all the way to the singularity then gives confidence in the numerical method. The variables for the 'first' interactive stage in equations (3.1) and (3.5) are related to those of the terminal-state variables in equations (2.13) by

$$\tilde{X} = (-t_I)^{-3/2} x_I, \quad \beta_I(x_I, t_I) = (-t_I)^{-1/4} \beta_0(\tilde{X}) = 2(-t_I)^{-1/4} \tilde{Y}_0(\tilde{X}). \quad (5.1a, b)$$

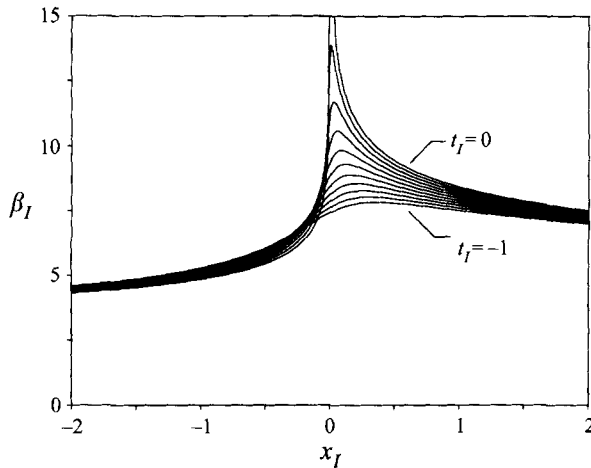


FIGURE 5. Calculated position of the upper shear layer β_I for the non-interactive case.

These equations give an exact result for the equation of the upper shear layer for any streamwise location x_I and time t_I , which then can be compared directly with the results of a non-interactive numerical integration. Calculations were carried out using the algorithm described in §4.2 using 401 points in the ξ -direction starting at $t_I = -1$. Since the pressure gradient is taken equal to zero in equation (3.18a), a value of t_{I0} need not be prescribed (since this only appears in the interaction condition (3.9)), and both the perturbations U_I and X_I in equations (3.18) remain unchanged for all t_I . Because of this behaviour, the choice of time step is inconsequential, and the central issue here is how well the numerical scheme for the continuity equation performs in producing distributions of $\beta_I(x_I, t_I)$ given exactly by equations (5.1). The equation of the upper shear layer from such a calculation at several times is shown in figure 5, and here the initial condition at $t_I = -1$ is the terminal solution. Subsequently, the upper shear layer compresses in the streamwise direction and grows away from the surface according to the scalings in equations (5.1) before becoming singular at $t_I = 0$. It may be noted that the integration scheme for the continuity equation reproduces the developing terminal solution very closely, and the computed and exact results are indistinguishable graphically. These results give confidence in the algorithm for integration of the continuity equation, and it is now possible to turn attention to the interactive problem.

In the 'first' interactive stage, the evolving terminal boundary-layer solution is altered by the influence of interaction, and for a numerical solution of this stage the time at which the calculation is initiated t_{I0} and the time step Δt_I must be chosen. Many calculations were carried out with different values of both parameters, and it was eventually determined that $t_{I0} = -50$ was sufficient to capture the bulk of the interaction and that the solution did not change for time steps smaller than $\Delta t_I = 0.001$. All results shown here were obtained using these values, and the effect of changes in these parameters on the numerical solution is discussed subsequently.

In view of the interactive boundary-layer calculations of Peridier *et al.* (1991b), it was anticipated at the outset of this work that the 'first' interactive stage would terminate in a singularity at a time prior to that occurring in the non-interactive case (i.e. the terminal solution). Indeed, for the mesh sizes used in the initial stages of the investigation, a singularity (as described in §3.2) always occurred at negative

Mesh	t_{Is}	\bar{t}_{Is}
$I_0 = 101, J_0 = 51, a = 1.0$	-0.005	-0.250
$I_0 = 201, J_0 = 101, a = 1.0$	-0.015	-0.750
$I_0 = 401, J_0 = 201, a = 1.0$	-0.029	-1.450

TABLE 1. Singularity times from calculations of the first interactive stage for various 'coarse' meshes.

times (i.e. $t_{Is} < 0$). In these cases the form of the singularity was essentially similar to that of the terminal solution shown in figure 5 except that the singularity always occurred at an earlier time. For example, singularity times for a few different meshes are given in table 1. These results appeared encouraging since the singularity time found by Peridier *et al.* (1991*b*) was approximately $\bar{t}_{Is} = -3.0$ (the exact value varied slightly with Reynolds number). As suggested by table 1, however, it subsequently proved impossible to obtain a grid-independent solution; as finer meshes were used, a singularity occurred at progressively earlier times.

As the mesh was refined further, an irregularity appeared in the solution, and results for a typical case are shown in figure 6 which were obtained using a mesh defined by $I_0 = 801, J_0 = 401$ and $a = 1.0$. Before describing the nature of the irregularity, some general features of the solution will be discussed. The position of the upper shear layer β_I shown in figure 6(*a*), evolves essentially as in the non-interactive case; the effect of the interaction is small globally. The pressure perturbation p_I induced by the growing boundary layer is shown in figure 6(*b*), where it may be noted that the magnitude is small due to the factor $(-t_{I0})^{-11/4}$ in the interaction condition (3.9). Figures 6(*c*) and 6(*d*) show the streamwise velocity perturbation and particle position perturbation, respectively, along the centreline $\hat{\eta} = 1$, and it is these perturbation quantities which most clearly reveal the overall effects of the interaction. Recall that the streamwise velocity function u_I becomes large near the upper and lower shear layers, as well as upstream and downstream of the interaction region. Consequently, the velocity perturbation, which is small in magnitude, only alters the flow appreciably in region II in the immediate vicinity of the centre of the domain, near the point $(\hat{\xi}, \hat{\eta}) = (0, 1)$, where the terminal-state velocity is small. Recall also that the terminal-state velocity along the central line is positive upstream of $(\hat{\xi}, \hat{\eta}) = (0, 1)$ and negative downstream of this point (cf. figure 2). With this in mind, the perturbation velocity (figure 6*c*) reveals an increasing positive perturbation just upstream of $\hat{\xi} \approx 0$ and a negative perturbation just downstream of this point. Thus, the interaction accelerates the focusing of the flow toward the eventual separation point at $x = x_s$; this suggests that the onset of the singularity would likewise be accelerated by interaction, which is consistent with the results of the coarse mesh calculations given in table 1.

In figures 6(*c*) and 6(*d*) it may be seen that there is an irregularity exhibited in the latter stages of the integration in the form of short-length-scale spikes centred near $\hat{\xi} \approx 0$ which form in the velocity perturbation and particle position perturbation distributions. Magnification of the pressure distribution near $\hat{\xi} \approx 0$ for this case (figure 6*b*) also reveals a slight irregularity. The effect of concentrating more points near $\xi = 0$, by reducing the value of the streamwise stretching parameter a in the finite-domain transformation (3.23), is shown in figure 7. These results were obtained on the same mesh used to obtain the results shown in figure 6 except for the value of a : figure 7(*a*) shows results for $a = 0.5$, and figure 7(*b*) shows results for $a = 0.25$.

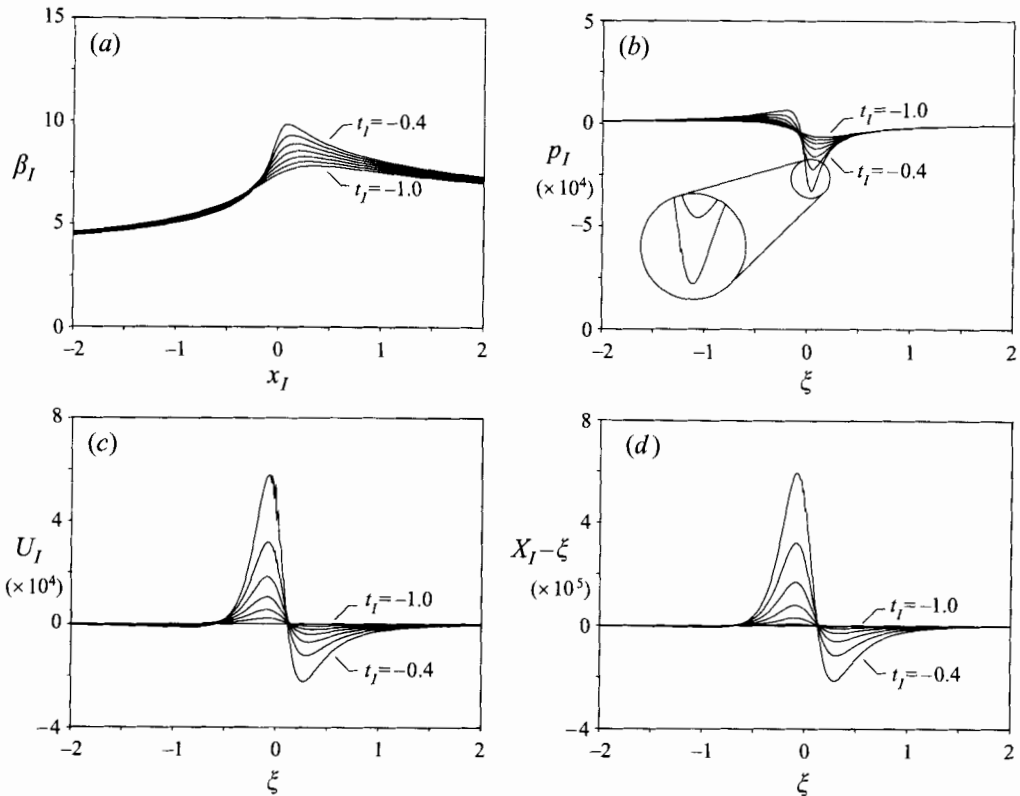


FIGURE 6. Interactive calculation with $a = 1.0$. (a) Equation of the upper shear layer β_I . (b) Induced pressure p_I . (c) Streamwise velocity perturbation U_I along centreline $\hat{\eta} = 1$. (d) Particle position perturbation $X_I - \xi$ along centreline $\hat{\eta} = 1$.

Note that halving the parameter a approximately doubles the number of points in the vicinity of $\xi = 0$. Comparing the results for the induced pressure in figure 7 with the case shown in figure 6(b), it becomes apparent that as more points are concentrated near $\xi = 0$, an instability occurs which is manifest at earlier times for finer meshes. This type of behaviour is reminiscent of the short-wavelength instability found by Ryzhov & Smith (1984) in considering dynamic stall and by Tutty & Cowley (1986) for triple-deck-type interactions; such an instability does not permit grid-independent solutions, because smaller step sizes in the mesh admit shorter-wavelength, faster-growing modes. This also accounts for the occurrence of the instability near $\xi = 0$, where the step sizes in physical space are smallest due to the transformation (3.23). The possible presence of an instability in the 'first' interactive stage is considered further in §6.

The effects of the other solution parameters on the calculated results support the physical existence of a high-frequency instability in the 'first' interactive stage. Increasing the number of points I_0 in the streamwise mesh was determined to have the same effect as reducing the stretching parameter a ; the smaller step sizes promote an earlier onset of the instability. The choice of an initial start time affects the spatial resolution, and the selection of t_{I0} involves a compromise. In general, the magnitude of t_{I0} should be large, but it follows from equations (3.5) that an increased value of $|t_{I0}|$ results in a reduced resolution in the streamwise direction in

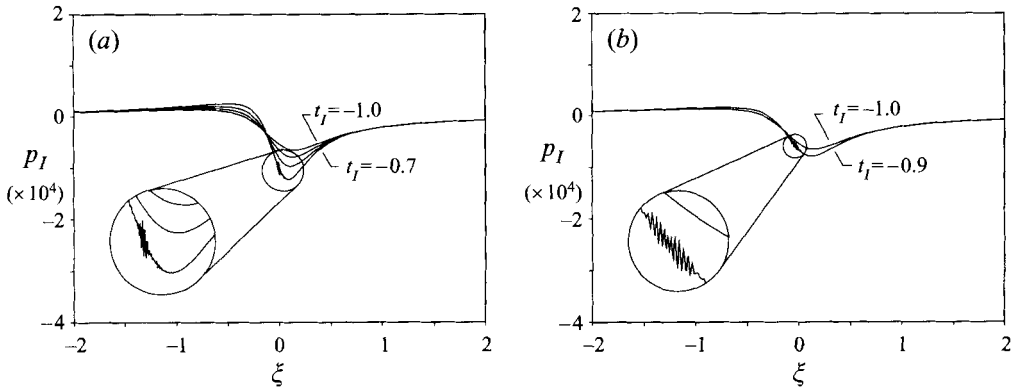


FIGURE 7. Induced pressure p_I from interactive calculations. (a) $a = 0.5$. (b) $a = 0.25$.

physical space. In an attempt to alleviate this difficulty, a remeshing procedure was carried out in which a calculation was performed successively over a series of time intervals starting from some large value of $|t_{I0}|$; the results of each previous interval (scaled according to equations (3.5)) were then used as initial conditions for the next interval with smaller $|t_{I0}|$. Although this procedure reduced the percentage of the interaction neglected (between $t_I = -\infty$ and t_{I0}), the effect on the instability was not noticeable, apparently because the instability is so highly mesh dependent. Of particular interest in numerical computations exhibiting instabilities is the effect of the time step Δt_I . It was found that reductions in the time step delayed slightly the onset of the instability, but it proved impossible to eliminate it completely through reducing the time step (cf. Ryzhov & Smith 1984; Tutty & Cowley 1986; Krasny 1986).

It is of interest to consider whether the instability can be suppressed through a smoothing technique as is routinely done in calculations of vortex-sheet motion (see, for example, Krasny 1986; Shelley 1992). In such problems numerical round-off error is known to have a catastrophic effect on the results, and successful smoothing was accomplished by application of a Fourier filter. After calculation of the discrete Fourier transform of the function, the Fourier coefficients with magnitude smaller than a prescribed value (which was set near the level of round-off of the computer) were set equal to zero. Alternatively, smoothing may be accomplished through convolution of the data function with a prescribed response function (see, for example, Press *et al.* 1989, pp. 407–414). This technique smooths out features in the data function which have length scales smaller than that of the response function thereby providing good control over the smoothing process. Here, smoothing was accomplished through convolution of the pressure distribution with a response function at each time step. A bell-shaped response function was used which was defined by $r(\xi) = b \exp(-d^2 \xi^2)$, where b sets the amplitude and d the length scale of the response function. The constant b was chosen such that the data function, in this case the pressure distribution, maintains the same scale before and after the convolution, and its particular value depends upon the computational mesh used. Adjusting d changes the width of the response function and, therefore, the level of smoothing; reducing d increases the width of the bell-shaped curve, which in turn increases the maximum length scale of features in the data function which are smoothed out. Solutions were sought which were independent of the level of smoothing as specified

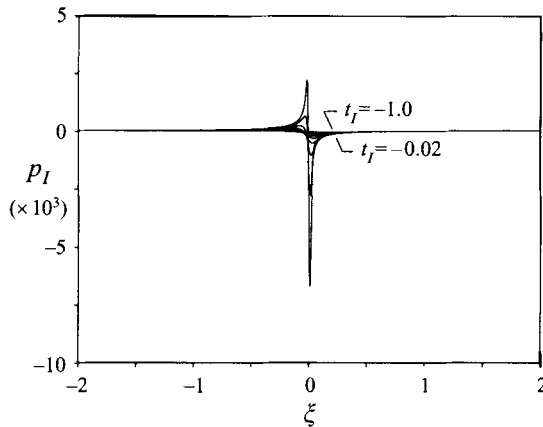


FIGURE 8. Induced pressure p_I from interactive calculation with smoothing: $d = 25$.

by d . The convolution was carried out at each time step by: (i) taking the fast Fourier transforms of both the pressure distribution and response function $r(\xi)$, (ii) multiplying the corresponding Fourier coefficients of these two functions to form a third function and (iii) computing the inverse transform of this function to obtain the smoothed pressure distribution which was then used in computing the momentum equation.

A series of calculations were carried out using this smoothing technique on the pressure distribution by specifying the response function with decreasing values of d . The mesh used for this case had $I_0 = 1024$, $J_0 = 512$ and $a = 0.25$. Although the number of grid points has been increased compared with the case shown in figure 7 (the convolution algorithm required 2^n grid points), the instability in the case with $d = 200$, for example, is much less severe and the solution breaks down at a much later time. By decreasing d further, the instability is gradually suppressed until eventually there is no evidence of the instability for values less than about $d = 25$ as shown in figure 8. The solution for cases in which the instability is completely suppressed then evolve toward a singularity in a manner similar to the non-interactive case and the coarse mesh results given in table 1. However, it was not possible to determine a solution which was grid independent and also independent of the level of smoothing (as specified by d); the singularity always occurred at times prior to the non-interactive singularity ($t_{Is} < 0$), but different singularity times were obtained for each d . Attempts to suppress the instability through smoothing are usually justified as corresponding to a hypothetical disturbance-free flow environment, but this has not been successful here. The question therefore remains as to the physical existence of the instability within the formulation of the 'first' interactive stage, and this is considered next.

6. Stability analysis

6.1. Linear stability

The numerical results described in §5 suggest that a high-frequency instability may be present within the 'first' interactive stage. To investigate this possibility, infinitesimal harmonic disturbances of amplitude $\epsilon \ll 1$ are introduced, and the temporal linear stability of the interactive stage (denoted by subscript zero) is considered (see similar

analyses given by Ryzhov & Smith 1984; Smith & Bodonyi 1985; Tutty & Cowley 1986; Brown *et al.* 1988). Therefore, define

$$u_I = u_0(x_I, Y_I, t_I) + \epsilon e^{i(\alpha x_I - \alpha c t_I)} u_1(x_I, Y_I, t_I) + \dots, \quad (6.1a)$$

$$\psi_I = \psi_0(x_I, Y_I, t_I) + \epsilon e^{i(\alpha x_I - \alpha c t_I)} \psi_1(x_I, Y_I, t_I) + \dots, \quad (6.1b)$$

$$p_I = p_0(x_I, t_I) + \epsilon e^{i(\alpha x_I - \alpha c t_I)} p_1(x_I, t_I) + \dots, \quad (6.1c)$$

$$\beta_I = \beta_0(x_I, t_I) + \epsilon e^{i(\alpha x_I - \alpha c t_I)} \beta_1(x_I, t_I) + \dots. \quad (6.1d)$$

Here, the wavenumber α is real and is assumed large ($\alpha \gg 1$) in accordance with the numerical results of §5; $c = c_r + ic_i$ is the complex wavespeed, and a disturbance is unstable if $c_i > 0$. Substituting the expressions (6.1) into the momentum equation (3.6a,b) and retaining the $O(\epsilon\alpha)$ terms the following equations are obtained for the perturbation functions:

$$(u_0 - c)u_1 - \psi_1 \frac{\partial u_0}{\partial Y_I} = -p_1, \quad u_1 = \frac{\partial \psi_1}{\partial Y_I}. \quad (6.2a, b)$$

Note that because α is large, equations (6.2) are the same as if the flow were plane parallel and u_0, u_1, ψ_0 and ψ_1 are functions of Y_I with β_0, β_1, p_0 and p_1 being constants. Substitution of equation (6.2b) into (6.2a) gives a first-order linear equation for ψ_1 which has the solution

$$\psi_1 = -p_1(u_0 - c) \int_0^{Y_I} \frac{dY_I}{(u_0 - c)^2}, \quad (6.3)$$

where an arbitrary function of integration must be zero to satisfy $\psi_1 = 0$ at $Y_I = 0$. Thus,

$$u_1 = \frac{\partial \psi_1}{\partial Y_I} = -p_1 \frac{\partial u_0}{\partial Y_I} \int_0^{Y_I} \frac{dY_I}{(u_0 - c)^2} - \frac{p_1}{u_0 - c}. \quad (6.4)$$

Substitution of the expansions (6.1a) and (6.1d) into the matching condition (3.7b) to the upper shear layer requires that

$$u_1 \sim \frac{8\beta_1}{(Y_I - \beta_0)^3} \quad \text{as } Y_I \rightarrow \beta_0, \quad (6.5)$$

for $\epsilon \ll 1$. Evaluating the solution (6.4) as $Y_I \rightarrow \beta_0$, it is easily shown using equations (3.7b) and (6.5) that

$$p_1 I_c = \beta_1, \quad I_c = \int_0^{\beta_0} \frac{dY_I}{(u_0 - c)^2}. \quad (6.6a, b)$$

Substitution of equations (6.1c) and (6.1d) into the interaction condition (3.9) gives

$$e^{i\alpha x_I} p_1 = -\frac{i\alpha(-t_{I0})^{-11/4}}{\pi} \int_{-\infty}^{\infty} \frac{\beta_1(s, t_I) e^{i\alpha s}}{x_I - s} ds, \quad (6.7)$$

which with $w = s - x_I$, may be written

$$p_1 = \frac{i\alpha(-t_{I0})^{-11/4}}{\pi} \int_{-\infty}^{\infty} \frac{\beta_1(x_I + w, t_I) e^{i\alpha w}}{w} dw. \quad (6.8)$$

The integral may be evaluated using contour integration and is equal to $\pi i \beta_1(x_I, t_I)$. Hence, the interaction condition requires that $p_1 = -(-t_{I0})^{-11/4} \alpha \beta_1$, and substituting this expression into equation (6.6a) gives the eigenvalue relation

$$(-t_{I0})^{-11/4} \alpha I_c = -1. \quad (6.9)$$

It follows that since α is real with $\alpha \gg 1$, I_c must also be real but small and negative; note that for the calculations and stability analysis, t_{I0} should be regarded as a large but $O(1)$ constant. In the present case, $u_0(Y_I)$ is symmetric about $Y_I = \beta_0/2$, and defining $\hat{Y}_I = 2Y_I/\beta_0$ the integral (6.6b) may be written

$$I_c = \beta_0 \int_0^1 \frac{d\hat{Y}_I}{(u_0 - c)^2}. \quad (6.10)$$

In this integral recall that c is complex, $u_0(x_I, Y_I, t_I)$ is a typical velocity profile and $\beta_0(x_I, t_I)$ is the distance to the upper shear layer at the x_I -location at which the velocity profile is considered.

6.2. Large- c instability

To determine if the flow is unstable, a solution is sought for the integral (6.10) using velocity profiles characteristic of the 'first' interactive stage to ascertain if there are values of the complex wavespeed c , with $c_i > 0$, for which I_c is small, real and negative. Because the integration range in equation (6.10) is finite, this suggests the following expansion:

$$I_c = \frac{\beta_0}{c^2} + \dots, \quad |c| \gg 1, \quad (6.11)$$

and thus for large c , the eigenvalue relation (6.9) gives $c_i = (-t_{I0})^{-11/8}(\beta_0\alpha)^{1/2}$, indicating a highly unstable situation with a growth rate given by

$$\Omega = \alpha c_i = (-t_{I0})^{-11/8}(\beta_0\alpha^3)^{1/2}. \quad (6.12)$$

Note that, apart from the constant $(-t_{I0})^{-11/8}$, this growth rate is the same as the linear stability case of Brown *et al.* (1988) (see their equation (2.8)). In view of the larger growth rate, this case would dominate any unstable points having $c = O(1)$, if they exist. It must be determined, however, whether the large- u_0 behaviour as $\hat{Y}_I \rightarrow 0$ affects the result (6.11) and thus the existence of the large- c instability.

To confirm the viability of the large- c instability, the integral (6.10) was evaluated numerically for typical velocity profiles $u_0(x_I, Y_I, t_I)$ and for a range of c . The numerical algorithm used to compute the integral (6.10) is due to Tutty & Cowley† (1986). Although the 'first' interactive stage is unsteady, the magnitude of the unsteady velocity perturbation is small (see figure 6c) and is not expected to qualitatively change the velocity profiles from the initial condition (i.e. the terminal solution). In the Eulerian formulation, the initial condition for the 'first' interactive stage at $t_I = -1$ is given in equations (3.8), and velocity profiles evolve from this solution during the 'first' interactive stage. Consequently, for the stability analysis it is sufficient to consider typical velocity profiles from the terminal solution. The integral (6.10) was evaluated over a range of c for velocity profiles at several streamwise locations, and the results were all qualitatively the same. Therefore, the results described are for the terminal solution at $x_I = 0$ (the centre of the domain). This is because the high-frequency oscillations were invariably observed in the full calculations near $x_I = 0$, where the streamwise velocities on the central line are smallest, and the motion is most susceptible to the pressure gradient induced by the interaction.

Contours of constant $\text{Im}(I_c)$ in the complex- c plane are shown in figure 9, which were obtained by calculating the integral (6.10) for a large number of complex values

† Equation (B2a) of their paper is corrected here to read $I_1 - I_0 \approx eh/(1+dh) + (g/d)\log(1+dh) + kh$.

of c . Note that since u_0 is very large as $\hat{Y}_1 \rightarrow 0$, the integrand approaches zero rapidly near the bottom shear layer. If unstable points exist, they must be located in the upper half-plane ($c_i > 0$) along lines where I_c is real, i.e. $\text{Im}(I_c) = 0$; one such line occurs in the upper half-plane which is indicated as A in figure 9(a). From the eigenvalue relation (6.9), a point along line A will be unstable if I_c is small and negative. Figure 9(b) shows the results for I_c for values of c along line A in figure 9(a) as well as the values predicted by the asymptotic expansion (6.11) for large c . It is evident that there are no unstable points along line A for $c = O(1)$ since the magnitude of I_c is rapidly increasing for decreasing c_i . On the other hand, I_c becomes small and negative with increasing c_i , and the numerical results do converge to the large- c prediction. These results confirm the presence of the large- c instability in the 'first' interactive stage. It is important to note that the instability is present even at the very onset of interaction and appears to be of an unusual type. Normally, instabilities are brought on by the development of an inflection point in a velocity profile; here, however, the primary features contributing to the instability are: (i) the presence of interaction and (ii) the existence of a shear layer within a finite distance of the wall. The large velocities that occur as $\hat{Y}_1 \rightarrow 0$ and $\hat{Y}_1 \rightarrow 2$ are not a significant feature of the instability. In contrast, the triple-deck cases considered by Tutty & Cowley (1986) require integration of equation (6.10) to be carried out across the semi-infinite range $(0, \infty)$ of the viscous sublayer, in which case the large- c instability of the present type is not possible.

7. Discussion

The numerical solution of the so-called 'first' interactive stage of unsteady boundary-layer separation has been considered in Lagrangian coordinates, and this stage has been shown to contain a high-frequency inviscid instability (similar to that found by Brown *et al.* 1988), which is manifest at the very onset of the viscous-inviscid interaction. This instability prevents the obtaining of a grid-independent solution, and as the grid is refined, the admittance of shorter-wavelength, faster-growing modes results in breakdown at progressively earlier times. Reductions in the time step delay, but do not suppress, the onset of the instability (see also Ryzhov & Smith 1984; Tutty & Cowley 1986; Krasny 1986). The presence of the instability was confirmed theoretically through a linear stability analysis. A condition for instability was derived and evaluated for typical velocity profiles over a range of the complex wavespeed c ; it was found that the instability can occur for large c . It should be emphasized that since the instability criterion was met in the initial condition (i.e. the terminal boundary-layer solution) of the first interactive stage, the instability is present as soon as the interaction comes into effect.

The present results appear to alter considerably current thinking of the physical picture of unsteady boundary-layer separation. Previously, a plausible sequence of events seemed to be as follows. As a boundary layer starts to separate, it evolves toward the terminal structure described by Van Dommelen & Shen (1982) and Elliott *et al.* (1983) until a time $O(Re^{-2/11})$ just prior to the formation of a non-interactive singularity when interaction with the outer inviscid flow becomes important. In this 'first' interactive stage, the solution would then evolve toward the interacting boundary-layer singularity of Smith (1988) at a time prior to the non-interactive singularity (Peridier *et al.* 1991*b*). At that juncture the effects of normal pressure gradient must then be taken into account in order to relieve the interacting boundary-layer singularity (Hoyle, Smith & Walker 1991).

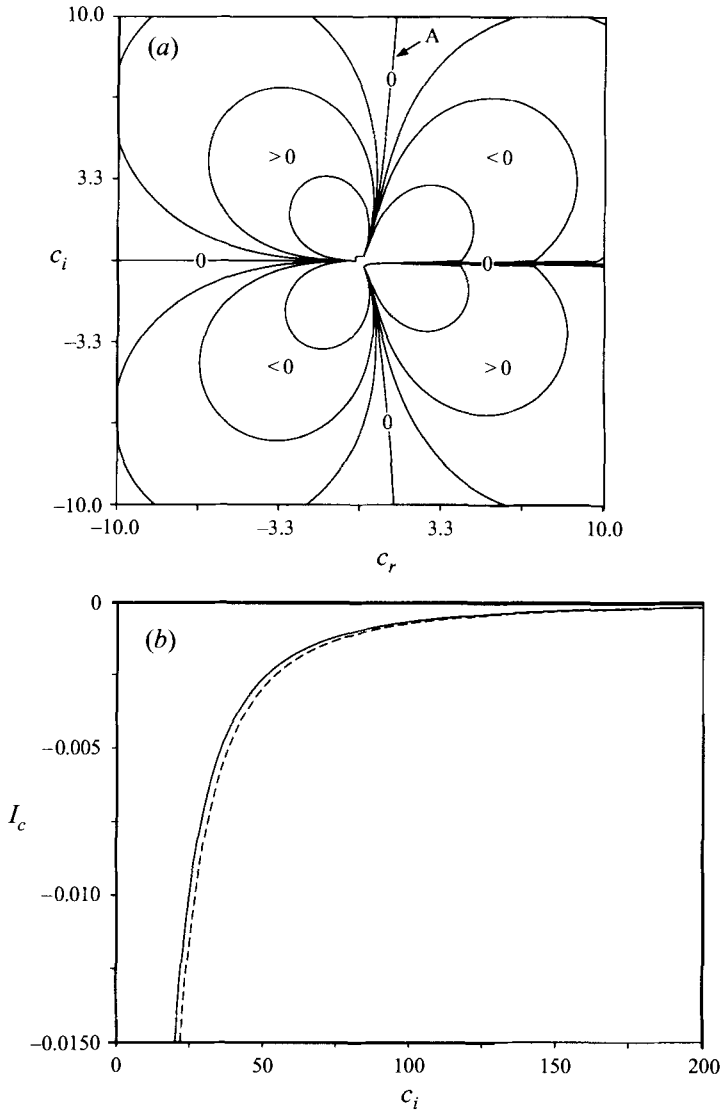


FIGURE 9. Numerical results for I_c . (a) Contours of constant $\text{Im}(I_c)$ on complex- c plane. (b) Comparison of analytical (-----) and numerical (——) results for I_c along line A in (a).

The current results, however, demonstrate that the 'first' interactive stage contains a short-wavelength instability, and that as a boundary layer focuses toward an eruption, the flow in the vicinity of the separation point becomes unstable at the onset of interaction with the external inviscid flow. This instability should also be present within conventional unsteady interacting boundary-layer solutions. However, it is not surprising that an instability was not encountered in the numerical calculations of Peridier *et al.* (1991b), because the instability occurs at short wavelengths in a structure having narrow streamwise extent embedded within the boundary layer. On the scales of the so-called 'first' interactive stage, the instability was only observed in the present study when computations with very high resolution were performed. A conventional interacting boundary-layer calculation, therefore, would require resolution in the separation region which probably is well beyond most current computational

resources. Instead, a condition analogous to equation (6.9) with (6.10) would need to be found and tested in order to determine if and when an instability occurred in an interacting boundary-layer calculation.

Because the present instability was found to exist at the very onset of the ‘first’ interaction, the question arises as to whether an instability develops prior to the non-interactive singularity time t_s , i.e. at times $t - t_s = O(1)$, where classical boundary-layer theory alone was thought to be dominant. It is possible that most calculations of unsteady boundary-layer separation carried out to date may not have sufficient resolution to pick up such an instability. The work of Smith & Elliott (1985) and Cowley, Hocking & Tutty (1985) suggests that an instability may occur in the classical boundary-layer equations when a point of zero shear stress develops within the boundary layer (see also, Bhaskaran *et al.* 1995). Recall that this is also an essential precursor to an unsteady separation event. The instability growth rates $O(\alpha^{1/2})$ of the Cowley–Hocking–Tutty and (at most) of the Smith–Elliott instabilities are relatively small, however, and the amplification of small disturbances may not have sufficient time to become manifest in a numerical calculation when the boundary layer rapidly evolves toward a finite-time singularity. Note that the growth rate in the present interactive instability is much larger and is $O(\alpha^{3/2})$. Even before the non-interactive instabilities described by Smith & Elliott (1985) and Cowley *et al.* (1985) occur, however, inflection points can develop in the unsteady boundary-layer profiles (see, for example, Peridier *et al.* 1991a); it is possible, therefore, that the integral criterion for breakup of the interactive solution described by Smith (1988) is met at some time $t = t_0$, which is $O(1)$ less than t_s . This suggests tentatively that the slightest amount of interaction can provoke the formation of the singularity of Smith (1988) at a time much earlier than the time t_s associated with the so-called ‘first’ interactive stage. Further study of these suggestions would seem to be worthwhile.

The authors wish to thank the referees for a number of useful comments and L. L. Van Dommelen in particular for noting a technical point in §3.2. This work was carried out while K.W.C. was supported by a National Defense Science and Engineering Graduate Fellowship. This work was supported by AFOSR under grants 89-0487, 92-J-0007 and F49620-93-1-0130. F.T.S. thanks the Army Research Office (grant no. DAALO3-92G0040) for support.

Appendix A. Solution of the terminal boundary-layer equations

The nonlinear equations (2.4) may be transformed to a first-order linear equation using Crocco variables in which \tilde{X} and \tilde{U} are adopted as independent variables, and the shear stress $\tau = \partial\tilde{U}/\partial\tilde{Y}$ is taken to be the dependent variable. In these variables, it is easily shown (Stewartson 1964) that $\partial\tilde{U}/\partial\tilde{X} = -\tau\partial\tilde{Y}/\tilde{X}$ and substitution in equation (2.4a) leads to

$$\frac{\partial\tilde{\Psi}}{\partial\tilde{X}} = -(\tilde{U} + M\tilde{X})\frac{\partial\tilde{Y}}{\partial\tilde{X}} - N\tilde{Y} - (M-1)\frac{\tilde{U}}{\tau}. \quad (\text{A } 1)$$

The continuity equation may be written in the form $\partial\tilde{U}/\partial\tilde{X} - \partial^2\tilde{\Psi}/\partial\tilde{X}\partial\tilde{Y} = 0$, and using equation (A 1), it is easily shown that τ satisfies

$$(\tilde{U} + M\tilde{X})\frac{\partial\tau}{\partial\tilde{X}} + (M-1)\tilde{U}\frac{\partial\tau}{\partial\tilde{U}} = (N + M - 1)\tau. \quad (\text{A } 2)$$

This is a first-order linear equation having the subsidiary equations

$$\frac{d\tilde{X}}{\tilde{U} + M\tilde{X}} = \frac{d\tilde{U}}{(M-1)\tilde{U}} = \frac{d\tau}{(N+M-1)\tau}. \tag{A 3}$$

Two independent integrals of these equations are

$$|\tau| = C|\tilde{U}|^{1+N/(M-1)}, \quad |\tilde{U}|^{M/(M-1)} = D|\tilde{U} + \tilde{X}|, \tag{A 4a, b}$$

where C and D are constants of integration, and the characteristic curves are given by equation (A 4b). The general solution obtained from equations (A 4) is

$$|\tilde{U}|^{1+N/(M-1)} = G(\phi)|\tau|, \quad \phi = \frac{|\tilde{U}|^{M/(M-1)}}{|\tilde{U} + \tilde{X}|}, \tag{A 5}$$

where $G(\phi)$ is an arbitrary function which is taken to be positive.

Appendix B. The interaction condition

In this Appendix interactive conditions for an unsteady flow over a surface defined as $y = 0$ will be described. First, consider the situation where the boundary layer has thickness $O(\delta)$ and the interaction occurs along a streamwise distance $O(1)$. In this circumstance the flow field at high Reynolds number is double structured consisting of: (i) an external flow described by coordinates (x, y) with corresponding velocity components (u, v) and (ii) a boundary layer where x is $O(1)$ with scaled normal distance and velocity defined by $Y = y/\delta$ and $V = v/\delta$, respectively. In the boundary layer, the normal velocity is given by

$$v = \delta V = -\delta \int_0^Y \frac{\partial u}{\partial x} dY, \tag{B 1}$$

and the boundary layer induces perturbations $O(\delta)$ in the external flow, where the expansions for the velocity components and pressure are of the form $(u, v, p) = (u_0, v_0, p_0) + \delta(u_1, v_1, p_1) + \dots$. Each of these terms are functions of (x, y, t) , and for a flow in which the leading-order inviscid flow is steady, the external flow has the form $u_0 \rightarrow U_e(x), v_0 \rightarrow -yU_e'(x)$ and $p_0 \rightarrow p_e(x)$ as $y \rightarrow 0$. Matching of the normal velocity requires that

$$v_1(x, 0, t) = \frac{\partial}{\partial x} [U_e(x, t)\delta^*(x, t)], \quad \delta^*(x, t) = \int_0^\infty \left[1 - \frac{u(x, Y, t)}{U_e(x, t)} \right] dY, \tag{B 2a, b}$$

where δ^* denotes the scaled dimensionless displacement thickness. The perturbation velocities $u_1(x, y, t)$ and $v_1(x, y, t)$ can be expressed in terms of a streamfunction which satisfies the Laplace equation in the upper half-plane since the external flow is assumed to be irrotational. The solution of this problem gives

$$u_1(x, 0, t) = \frac{1}{\pi} \int_{-\infty}^\infty v_1(s, 0, t) \frac{ds}{x-s}, \tag{B 3}$$

where the integral is a Cauchy principle-value integral. It follows from the Bernoulli equation for unsteady flow evaluated near the surface that $p_1(x, 0, t) + U_e(x, t)u_1(x, 0, t) + \partial\phi_1/\partial t = 0$ to leading order, where $u_1 = \partial\phi_1/\partial x$ and ϕ_1 is a velocity perturbation potential. Differentiation of this equation with respect to x and using equations (B 2)

and (B 3) leads to

$$\begin{aligned} \frac{\partial p_1}{\partial x} = & -\frac{1}{\pi} \int_{-\infty}^{\infty} \frac{\partial^2}{\partial s \partial t} (U_e \delta^*) \frac{ds}{x-s} - \frac{U_e(x, t)}{\pi} \int_{-\infty}^{\infty} \frac{\partial^2}{\partial s^2} (U_e \delta^*) \frac{ds}{x-s} \\ & - \frac{1}{\pi} \frac{dU_e}{dx} \int_{-\infty}^{\infty} \frac{\partial}{\partial s} (U_e \delta^*) \frac{ds}{x-s}. \end{aligned} \quad (\text{B } 4)$$

Now consider the pressure-displacement relation for the 'first' interactive stage discussed in §3.1. In the physical coordinate y , the equation for the upper shear layer is $y = \eta(x, t) = Re^{-5/11} A \phi_0^{-1/4} \bar{\beta}_I(\bar{x}_I, \bar{t}_I)$, where \bar{x}_I and \bar{t}_I are defined in equations (3.1), and it is evident that $\eta \ll 1$ as $Re \rightarrow \infty$. The kinematic condition $v = \partial \eta / \partial t + u \partial \eta / \partial x$ gives the normal velocity at the boundary-layer edge. Since the interaction is localized near $x = x_s$ as an eruption starts to develop, u may be replaced by $U_s = U_e(x_s)$, and it follows from equations (3.1) that to leading order $v = Re^{-2/11} A \phi_0^{-3/4} (U_s + K) \partial \bar{\beta}_I / \partial \bar{x}_I$ is the normal velocity induced by the thickening boundary layer. Note that the contribution due to the time derivative is $O(Re^{-3/11})$ and thus is negligible with respect to the term retained in v as $Re \rightarrow \infty$. Therefore, in a coordinate system drifting upstream with velocity $-K$, a local interaction zone having dimensions $O(Re^{-3/11})$ by $O(Re^{-3/11})$ forms near x_s , where the perturbations in velocity and pressure are $O(Re^{-2/11})$.

In this interaction region, define

$$u = U_s + K + Re^{-2/11} \tilde{u}_1(\bar{x}_I, \bar{y}, \bar{t}_I) + \dots, \quad v = Re^{-2/11} \tilde{v}_1(\bar{x}_I, \bar{y}, \bar{t}_I) + \dots, \quad (\text{B } 5a, b)$$

$$p = p_s + Re^{-2/11} \phi_0 \tilde{p}_1(\bar{x}_I, \bar{y}, \bar{t}_I) + \dots, \quad (\text{B } 5c)$$

where p_s and U_s are the limiting values of $p_e(x)$ and $U_e(x)$ as $x \rightarrow x_s$; the independent variables are given in equations (3.1a), (3.1c) and $\bar{y} = Re^{3/11} \phi_0^{-1/2} y$. The constant ϕ_0 has been included in equation (B 5c) to make the expansion consistent with (3.1e) in the boundary layer. Substitution into the Navier–Stokes equations yields

$$\frac{\partial \tilde{u}_1}{\partial \bar{x}_I} + \frac{\partial \tilde{v}_1}{\partial \bar{y}} = 0, \quad (U_s + K) \frac{\partial \tilde{u}_1}{\partial \bar{x}_I} = -\phi_0 \frac{\partial \tilde{p}_1}{\partial \bar{x}_I}, \quad (U_s + K) \frac{\partial \tilde{v}_1}{\partial \bar{x}_I} = -\phi_0 \frac{\partial \tilde{p}_1}{\partial \bar{y}}. \quad (\text{B } 6a, b, c)$$

This system of equations leads to the Laplace equation for the perturbation stream-function $\tilde{\psi}_1$, where $\tilde{u}_1 = \partial \tilde{\psi}_1 / \partial \bar{y}$, $\tilde{v}_1 = -\partial \tilde{\psi}_1 / \partial \bar{x}_I$, and the solution gives a result analogous to equation (B 3) at the outer edge of region II. From equations (B 5b) and (B 6b), it may easily be shown that

$$\tilde{p}_1(\bar{x}_I, 0, \bar{t}_I) = -A \phi_0^{-7/4} (U_s + K)^2 \frac{1}{\pi} \int_{-\infty}^{\infty} \frac{\partial \bar{\beta}_I}{\partial s} \frac{ds}{\bar{x}_I - s}. \quad (\text{B } 7)$$

By defining the reference velocity suitably, it is possible to have $A \phi_0^{-7/4} (U_s + K)^2 = 1$ thereby giving the interaction condition (3.4) in dimensionless form.

REFERENCES

- ABRAMOWITZ, M. & STEGUN, I. A. 1964 *Handbook of Mathematical Functions*. US Government Printing Office, Washington, DC.
- ACARLAR, M. S. & SMITH, C. R. 1987a A study of hairpin vortices in a laminar boundary layer. Part 1. Hairpin vortices generated by hemisphere protuberances. *J. Fluid Mech.* **175**, 1–41.
- ACARLAR, M. S. & SMITH, C. R. 1987b A study of hairpin vortices in a laminar boundary layer. Part 2. Hairpin vortices generated by fluid injection. *J. Fluid Mech.* **175**, 43–83.

- BHASKARAN, R., SMITH, F. T. & TIMOSHIN, S. N. 1995 The appearance of boundary-layer instabilities as a velocity minimum develops. *Proc. R. Soc. Lond. A* **451**, 331–339.
- BOUARD, R. & COUTANCEAU, M. 1980 The early stage of development of the wake behind an impulsively-started cylinder for $40 < Re < 10^4$. *J. Fluid Mech.* **101**, 583–607.
- BROWN, S. N., CHENG, H. K. & SMITH, F. T. 1988 Nonlinear instabilities and break-up of separated flow. *J. Fluid Mech.* **193**, 191–216.
- CASSEL, K. W. 1993 The effect of interaction on boundary-layer separation and breakdown. PhD Dissertation, Lehigh University.
- CEBECI, T. 1982 Unsteady separation. In *Numerical and Physical Aspects of Aerodynamic Flows* (ed. T. Cebeci), pp. 265–277. Springer.
- CHUANG, F. S. & CONLISK, A. T. 1989 Effect of interaction on the boundary layer induced by a convected rectilinear vortex. *J. Fluid Mech.* **200**, 337–365.
- COLLINS, W. M. & DENNIS, S. C. R. 1973 Flow past an impulsively-started circular cylinder. *J. Fluid Mech.* **60**, 105–127.
- COWLEY, S. J., HOCKING, L. M. & TUTTY, O. R. 1985 The stability of solutions of the classical unsteady boundary-layer equations. *Phys. Fluids* **28**, 441–443.
- COWLEY, S. J., VAN DOMMELEN, L. L. & LAM, S. T. 1990 On the use of Lagrangian variables in descriptions of unsteady boundary-layer separation. *Phil. Trans. R. Soc. Lond. A* **333**, 343–378.
- DOLIGALSKI, T. L., SMITH, C. R. & WALKER, J. D. A. 1994 Vortex interactions with walls. *Ann. Rev. Fluid Mech.* **26**, 573–616.
- DOLIGALSKI, T. L. & WALKER, J. D. A. 1984 The boundary layer induced by a convected two-dimensional vortex. *J. Fluid Mech.* **139**, 1–28.
- ELLIOTT, J. W., COWLEY, S. J. & SMITH, F. T. 1983 Breakdown of boundary layers: (i) on moving surfaces; (ii) in semi-similar unsteady flow; (iii) in fully unsteady flow. *Geophys. Astrophys. Fluid Dyn.* **25**, 77–138.
- HEAD, M. R. & BANDYOPADHYAY, P. 1981 New aspects of turbulent boundary-layer structure. *J. Fluid Mech.* **107**, 297–338.
- HENKES, R. A. W. M. & VELDMAN, A. E. P. 1987 On the breakdown of the steady and unsteady interacting boundary-layer description. *J. Fluid Mech.* **179**, 513–529.
- HOYLE, J. M., SMITH, F. T. & WALKER, J. D. A. 1991 On sublayer eruption and vortex formation. *Comput. Phys. Commun.* **65**, 151–157.
- KRASNY, R. 1986 A study of singularity formation in a vortex sheet by the point-vortex approximation. *J. Fluid Mech.* **167**, 65–93.
- LAM, S. T. 1988 On high-Reynolds-number laminar flows through a curved pipe, and past a rotating cylinder. PhD Dissertation, University of London.
- MCCROSKY, W. J. 1982 Unsteady airfoils. *Ann. Rev. Fluid Mech.* **14**, 285–311.
- PERIDIER, V. J., SMITH, F. T. & WALKER, J. D. A. 1991a Vortex-induced boundary-layer separation. Part 1. The unsteady limit problem $Re \rightarrow \infty$. *J. Fluid Mech.* **232**, 99–131.
- PERIDIER, V. J., SMITH, F. T. & WALKER, J. D. A. 1991b Vortex-induced boundary-layer separation. Part 2. Unsteady interacting boundary-layer theory. *J. Fluid Mech.* **232**, 133–165.
- PRESS, W. H., FLANNERY, B. P., TEUKOLSKY, S. A. & VETTERLING, W. T. 1989 *Numerical Recipes, The Art of Scientific Computing*. Cambridge University Press.
- RILEY, N. & VASANTHA, R. 1989 Unsteady high-Reynolds-number flows. *J. Fluid Mech.* **205**, 243–262.
- RYZHOV, O. S. & SMITH, F. T. 1984 Short-length instabilities, breakdown and initial value problems in dynamic stall. *Mathematika* **31**, 163–177.
- SEARS, W. R. & TELIONIS, D. P. 1975 Boundary-layer separation in unsteady flow. *SIAM J. Appl. Maths* **28**, 215–235.
- SHELLEY, M. J. 1992 A study of singularity formation in vortex-sheet motion by a spectrally accurate vortex method. *J. Fluid Mech.* **244**, 493–526.
- SMITH, C. R., WALKER, J. D. A., HAIDARI, A. H. & SOBRUN, U. 1991 On the dynamics of near-wall turbulence. *Phil. Trans. R. Soc. Lond. A* **336**, 131–175.
- SMITH, F. T. 1982 On the high Reynolds number theory of laminar flows. *IMA J. Appl. Maths* **28**, 207–281.
- SMITH, F. T. 1988 Finite-time break-up can occur in any unsteady interacting boundary layer. *Mathematika* **35**, 256–273.
- SMITH, F. T. & BODONYI, R. J. 1985 On short-scale inviscid instabilities in flow past surface-mounted obstacles and other non-parallel motions. *Aero. Q.* June/July.

- SMITH, F. T. & ELLIOTT, J. W. 1985 On the abrupt turbulent reattachment downstream of leading-edge laminar separation. *Proc. Roy. Soc. Lond. A* **401**, 1–27.
- STEWARTSON, K. 1964 *The Theory of Laminar Boundary Layers in Compressible Fluids*. Oxford University Press.
- TUTTY, O. R. & COWLEY, S. J. 1986 On the stability and the numerical solution of the unsteady interactive boundary-layer separation. *J. Fluid Mech.* **168**, 431–456.
- VAN DOMMELEN, L. L. 1981 Unsteady boundary-layer separation. PhD Dissertation, Cornell University.
- VAN DOMMELEN, L. L. 1991 Lagrangian description of unsteady separation. *Lect. Appl. Maths* **28**, 701–718.
- VAN DOMMELEN, L. L. & SHEN, S. F. 1980 The spontaneous generation of the singularity in a separating laminar boundary layer. *J. Comput. Phys.* **38**, 125–140.
- VAN DOMMELEN, L. L. & SHEN, S. F. 1982 The genesis of separation. In *Numerical and Physical Aspects of Aerodynamic Flows* (ed. T. Cebeci), pp. 293–311. Springer.
- WALKER, J. D. A. 1978 The boundary layer due to a rectilinear vortex. *Proc. R. Soc. Lond. A* **359**, 167–188.
- WALKER, J. D. A. 1990 Models based on the dynamical features of the wall layer. *Appl. Mech. Rev.* **43**, S232–S239.